

SHAPE EXTRACTION USING PHOTOGRAPHIC TOMOGRAPHY



A THESIS SUBMITTED IN PARTIAL FULFILMENT
OF THE REQUIREMENT FOR THE DEGREE OF
MASTER ENGINEERING IN ELECTRONICS ENGINEERING
SCHOOL OF GRADUATE STUDIES
KING MONGKUT'S INSTITUTE OF TECHNOLOGY LADKRABANG

2003

ISBN 974 - 324 - 597 - 9

เลขหน้.....
เลขทะเบียน..... 41527
วัน, เดือน, ปี..... 30 ส.ค. 2547

.b.....
.i.....



COPYRIGHT 2003

SCHOOL OF GRADUATE STUDIES

KING MONGKUT'S INSTITUTE OF TECHNOLOGY LADKRABANG

This material is reserved for educational use only, not allowed for commercial use.

Forbidden to modify the content, and cite the document when use.

หัวข้อวิทยานิพนธ์	การหาโครงร่างของวัตถุโดยใช้หลักการโทโมกราฟีกับภาพถ่าย
นักศึกษา	นายวิวัฒน์ วิทยชานาญกุล
รหัสนักศึกษา	44061312
ปริญญา	วิศวกรรมศาสตรมหาบัณฑิต
สาขาวิชา	วิศวกรรมอิเล็กทรอนิกส์
พ.ศ.	2546
อาจารย์ผู้ควบคุมวิทยานิพนธ์	รศ.ดร.มนัส สัจวรศิลป์
อาจารย์ผู้ควบคุมวิทยานิพนธ์ร่วม	ศ.ดร.ชูชาติ ปิณฑวิรุจน์

บทคัดย่อ

โทโมกราฟีคือกระบวนการสร้างภาพตัดขวางของวัตถุโดยไม่ทำให้วัตถุเสียหาย ข้อมูลดิบของกระบวนการนี้ถูกเรียกว่าภาพโปรเจกชัน ซึ่งโดยปกติแล้วได้มาจากการแผ่คลื่นในย่านความถี่จำกัดทะลุผ่านวัตถุที่มุมต่างๆกันแล้วรับด้วยแผงของตัวรับคลื่นในด้านตรงข้าม สำหรับในงานวิจัยนี้ภาพโปรเจกชันจากคลื่นความถี่ได้ถูกแทนที่ด้วยภาพถ่ายของวัตถุภายใต้สภาพแสงปกติที่มุมต่างๆ เมื่อผ่านกระบวนการโทโมกราฟีแล้ว ข้อมูลที่ได้จะเป็นชุดของภาพตัดขวางเสมือน ซึ่งส่วนในของภาพตัดขวางไม่ใช่ของจริงเพียงแต่ขอบของมันเท่านั้นที่ต้องการ ค่าพารามิเตอร์ที่ใช้ในกระบวนการได้แก่ ชนิดของอัลกอริธึม, จำนวนภาพโปรเจกชัน, และระยะห่างระหว่างวัตถุกับส่วนรับภาพได้ถูกศึกษาอย่างละเอียด ชุดของภาพตัดขวางเสมือนนี้สามารถนำไปใช้ในงานได้หลายลักษณะ อย่างเช่น การทำภาพสามมิติของวัตถุหรือการวัดขนาดของวัตถุเป็นต้น นอกจากนี้ยังมีการเสนอวิธีการแก้ไขปัญหาสำหรับวัตถุที่พื้นผิวบางส่วนถูกบัง อย่างไรก็ตามสำหรับวัตถุที่พื้นผิวทั้งหมดถูกบังนั้นไม่สามารถแก้ไขได้ เพราะพื้นผิวส่วนนั้นจะไม่ปรากฏในภาพโครงร่างเลย

Thesis Title	Shape Extraction Using Photographic Tomography
Student	Mr.Withawat Withayachumnankul
Student ID.	44061312
Degree	Master of Engineering
Programme	Electronics Engineering
Year	2003
Thesis Advisor	Assoc.Prof.Dr.Manas Sangworasil
Thesis Co-Advisor	Asst.Prof.Dr.Chuchart Pintavirooj

ABSTRACT

Tomographic imaging is a technique for exploring a cross-section of an inspected object without destruction it. Raw data of this process, known as the projections, are normally achieved by repeatedly radiating coherent waveforms through the object in a number of viewpoints, and receiving them using an array of corresponding detector in the opposite position. In this research, as a replacement of radiographs, a series of photographs taken around the opaque object under the ambient light is completely served as the projections. From the process of tomography, the outcome is the stack of pseudo cross-sectional image, not the internal of which is authentic, but the edge or contour is valid. The parameters of the process, including the type of algorithm, the number of projections, and the distance from the object to the projection plane, are investigated comprehensively. Several applications can implicitly take advantages from the stack of contour, for instance, 3D modeling and geometric measurements. Also the correction scheme for partially concave occlusion of the object is brought up. Nevertheless, the process has a problem to extract the totally-concave-occlusion shape since the concave area does not express itself on the outline of any projection.

Acknowledgements

Along the great journey of this thesis, I have been facing with both the hard times and the good times. Someone helped me in the hard times, someone applauded me in the good times, and someone encouraged me while I felt desperate. Without them, I would not have made it this far. At this point, I would like to express my appreciation to these companions.

My parents for being supportive in everything, and both of them are the heroes for me. My great advisors, Assoc.Prof.Dr. Manas Sangworasil and Asst.Prof.Dr. Chuchart Pintavirooj, for giving me a great deal of invaluable suggestions and concepts, including the heart of being a good researcher. Dr. Supan Tungjikusolmun, Dr. Kitiphol Chitsakul, Asst.Prof. Pichai Koosirivanichakorn, and Assoc.Prof.Dr. Surapan Airphaiboon for their helpful comments both in and out of the course. Mr. Chinnapat Nantajiwakornchai and Mr. Polsart Lertprasert for assembling the significant equipment, the rotating platform and imaging unit.

Mr. Kasemsuk Sepsirisuk for guiding me the surface and volume rendering techniques, and sharing me the workplace. Ms. Chanatip Ninkeaw for providing much assistance along my first step. Mr. Phittaya Ungpinitpong for being an affable colleague and excellent debugger. Mr. Chanrit Yossontikul for supplying the ECT data. Ms. Sinaporn Suebvisai for supporting the key literatures. Ms. Piyanuch Sommani for marching along with me through all the troubles. The junior staffs of Biomedical Signal and Image Processing laboratory and B-204 for their helpfulness.

Most of my researching fund has been kindly supported by the Japan International Cooperation Agency (JICA), and the School of Graduate Studies, KMITL.

Withawat Withayachumnankul

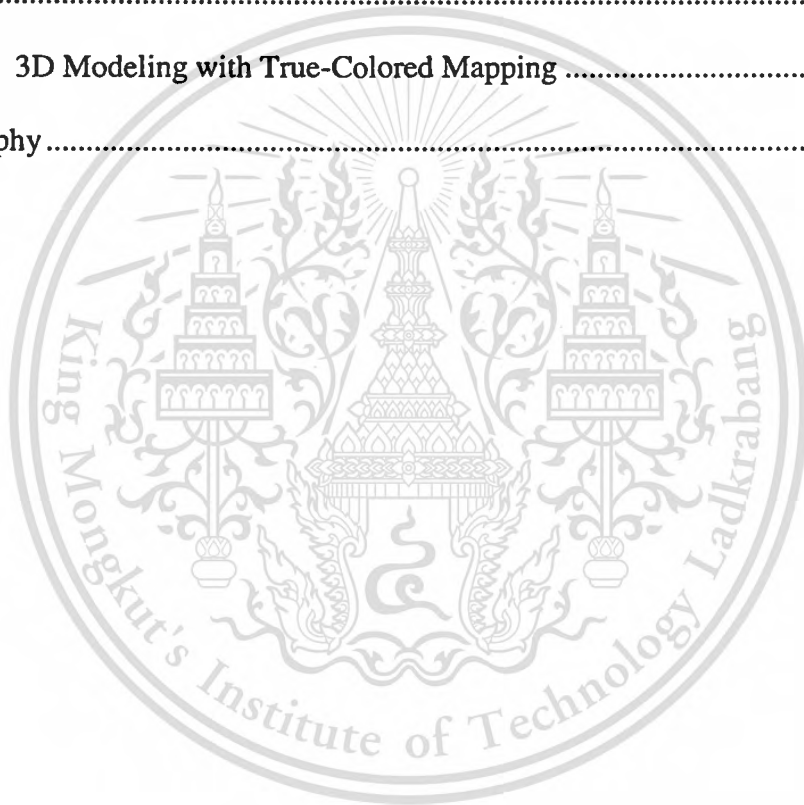
Table of Contents

	Page
Thai Abstract	I
English Abstract	II
Acknowledgements	III
Table of Contents.....	IV
List of Tables	VI
List of Figures.....	VII
Abbreviation	X
Chapter 1 Introduction	1
1.1 Significance of the Problems.....	1
1.2 Objective.....	1
1.3 Hypothesis	1
1.4 Chapter Organizing.....	2
Chapter 2 Tomography & Shape Extraction.....	3
2.1 Tomography – Concept and Applications.....	3
2.2 Shape Extraction Techniques	4
2.3 Shape Extraction Using Photographic Tomography – The Reviews	5
Chapter 3 Tomographic Imaging for Non-Diffracting Source.....	7
3.1 Parallel-Beam Tomography.....	7
3.1.1 Parallel-Beam Projection.....	7
3.1.2 Fourier Slice Theorem.....	8
3.1.3 Filtered-Backprojection Algorithm	9
3.2 Cone-Beam Tomography	11
3.2.1 Cone-Beam Projection.....	11
3.2.2 Cone-Beam Backprojection.....	13
3.3 Algebraic Formulation.....	13
Chapter 4 Modified Tomography for Silhouetted Projections.....	15
4.1 Modified Tomography.....	15
4.1.1 Camera System and Cone-Beam Projection.....	15
4.1.2 Modified Reconstruction Algorithm	16
4.1.3 Shape Extraction Process.....	18
4.2 Patch’s Occlusion	20
4.2.1 Concave Occlusion	20
4.2.2 Perspective Occlusion.....	21
4.3 Imaging Unit.....	21
Chapter 5 Evaluation of the Reconstruction	23
5.1 Optimum Conditions of the Reconstruction.....	23
5.1.1 Reconstruction Technique	24
5.1.2 Number of Projections.....	26
5.1.3 Reconstruction Geometry	30
5.2 Practical Implementation.....	32

This material is reserved for educational use only, not allowed for commercial use.

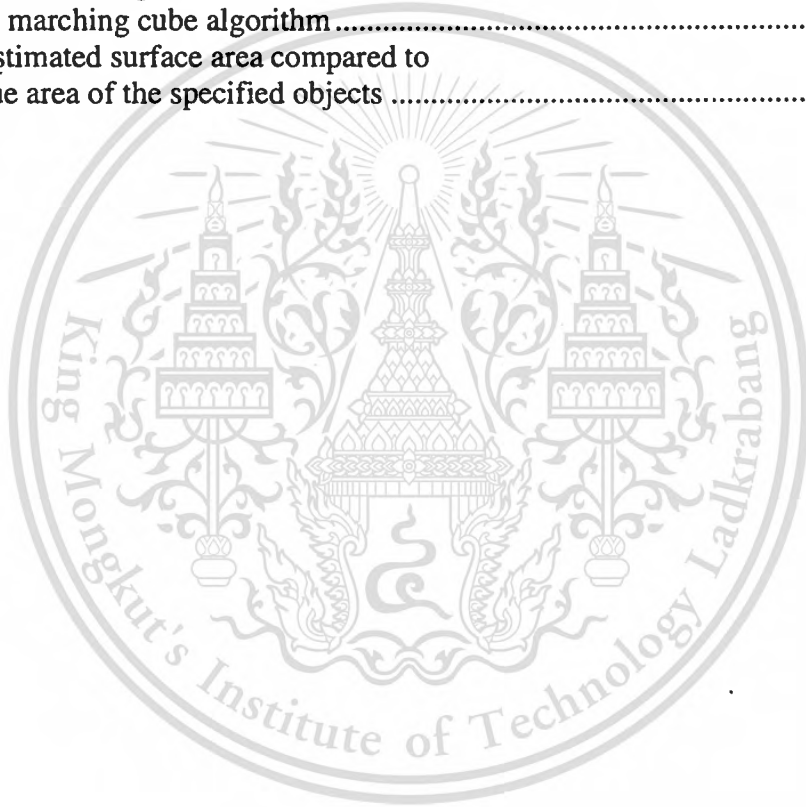
Forbidden to modify the content and cite the document when use.

5.3	Improving Scheme for Concave Object	35
5.3.1	Simulation.....	35
5.3.2	Implementation.....	37
Chapter 6	Applications.....	39
6.1	3D Modeling.....	39
6.2	Geometric Measurements.....	47
6.2.1	Volume Measurement.....	47
6.2.2	Surface Measurement	49
Chapter 7	Conclusions and Suggestions	51
7.1	Conclusions	51
7.2	Suggestions.....	51
References	52
Appendix	3D Modeling with True-Colored Mapping	56
Autobiography	59



List of Tables

Table	Page
5.1 MSE and time usage of the reconstructed cross sections by different reconstruction techniques	24
5.2 MSE and time usage of the reconstructed cross sections with different numbers of projections by the MBP	28
5.3 MSE of the reconstructed models with different distances of projections	30
5.4 MSE of the reproduced (normal) and synthesized (italic) projections	34
5.5 MSE of the reconstructed models by different axes of rotation	36
6.1 The attributes of the reconstructed objects	40
6.2 The estimated volume compared to the true volume of the specified objects	48
6.3 The area of triangles contained in each cube created by the marching cube algorithm	49
6.4 The estimated surface area compared to the true area of the specified objects	50



List of Figures

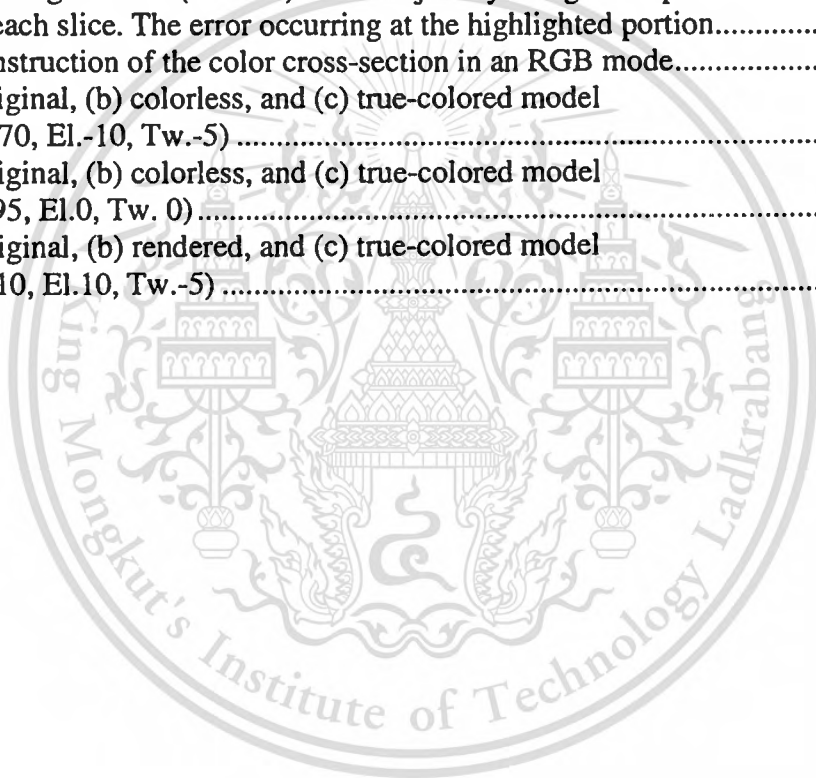
Figure	Page
1.1 The photographic tomography's process.....	1
2.1 Medical imaging – Cross sections of the human brain from MRI (left), and CT (right) [8]	3
2.2 Seismic exploration – Cutaway views of the earth [9].....	4
2.3 Industrial measurement – Flame imaging using an electrical capacitance tomography [10]	4
2.4 Nondestructive testing – Tomographic image showing soldering irregularities inside the IC [11]	4
2.5 The Laser Plane Range Finder and 3D result [15]	5
2.6 Synthetic vase and its depth map using the shape from shading [18].....	5
3.1 Parallel-beam projection of function $f(x, y)$ at angle θ	8
3.2 The relationship between the projection of the object and the Fourier transform of the object function	9
3.3 The concept of reconstruction by backprojection.....	10
3.4 3D parallel-beam geometry	12
3.5 Cone-beam geometry.....	12
3.6 Algebraic Reconstruction Technique, each cell representing an unknown variable in the linear equations	14
4.1 The ordinary optical system [36].....	15
4.2 Parallel-beam backprojection of silhouetted projections.....	16
4.3 The pseudo cross-sections, (a) before enhancement, and (b) after enhancement	17
4.4 The process diagram of the photographic tomography	18
4.5 Examples of pseudo cross sections.....	18
4.6 The montage of silhouetted projections in the half plane.....	19
4.7 The montage of cross sections displayed at every 5 layers	19
4.8 Three cross-sections giving the same reconstructed image [36]. The shaded zones are the occluded area, and the solid dots are the dominating points	20
4.9 Cubes showing two types of occlusions, (a) partially-concave occlusion and (b) totally-concave occlusion. The marker indicating the totally-occluded area	20
4.10 (a) 2D perspective projections at the distance of $2x$ from the center of cube and (b) the erroneously reconstructed cube because of the occlusion on the top and bottom (Az. -15 , El. 0).....	21
4.11 The prototype of an imaging unit for acquiring the sequence of photographs consisting of digital camera and rotating platform placed on dual rails	22
5.1 The CG cross sections representing various patterns, (a) the ellipse, (b) the rectangle, (c) the blob, and (d) the multi-circles	23
5.2 The ellipses reconstructed by each technique, (a) prototype, (b) FBP, (c) MBP, and (d) ART	25
5.3 The rectangles reconstructed by each technique, (a) prototype, (b) FBP, (c) MBP, and (d) ART	25
5.4 The blobs reconstructed by each technique, (a) prototype, (b) FBP, (c) MBP, and (d) ART	25

This material is reserved for educational use only, not allowed for commercial use.

Figure	Page
5.5 The multi-circles reconstructed by each technique, (a) prototype, (b) FBP, (c) MBP, and (d) ART	25
5.6 The ellipses reconstructed from different numbers of projections (without threshold), (a) 2, (b) 4, (c) 9, and (d) 20	27
5.7 The rectangles reconstructed from different numbers of projections (without threshold), (a) 2, (b) 4, (c) 9, and (d) 20	27
5.8 The blobs reconstructed from different numbers of projections (without threshold), (a) 2, (b) 4, (c) 9, and (d) 20	27
5.9 The multi-circles reconstructed from different numbers of projections (without threshold), (a) 5, (b) 6, (c) 9, and (d) 20. A rapid dropping of the error occurring in (b).....	27
5.10 Plotting of the MSE and time usage against the number of projections for all of the cross sections	29
5.11 3D models used to simulate the reconstruction geometry (a) the ellipse (Az. -20, El. -5), (b) the cube (Az. -25, El. -5)	30
5.12 3D reconstructed models at a distance of 16x (a) the ellipse (Az. -20, El. -5), (b) the cube (Az. -25, El. -5)	31
5.13 Reprojection strategy	32
5.14 Comparing of the synthesized projection to the original projection of the mannequin at degree 4, (a) original, (b) synthesized, and (c) synthesized pasted over original	33
5.15 Plotting of MSE of reproduced and synthesized projections against angle of projections (the data are fitted by 6th order polynomial).....	34
5.16 CG concave models for simulation (a) the holed cube (Az -15, El -15), (b) the jointed tori (Az -10, El 0), and (c) the Boston teapot (Az -15, El -25)	35
5.17 The holed cubes reconstructed from the rotation with respect to, (a) X axis, (b) Y axis, and (c) $X \cap Y$	36
5.18 The jointed tori reconstructed from the rotation with respect to, (a) X axis, (b) Z axis, and (c) $X \cap Z$	36
5.19 The Boston teapot reconstructed from the rotation with respect to, (a) Y axis, (b) Z axis, and (c) $Y \cap Z$	36
5.20 The cutaway views at x of 128 of (a) the original teapot, (b) the $X \cap Y \cap Z$ teapot, showing the flaws to reconstruct a totally-concave object	37
5.21 Original wood cat, (a) side view and (b) top view	38
5.22 First reconstructed model along Z axis, (a) side view and (b) top view.....	38
5.23 Second reconstructed model along X axis, (a) side view and (b) top view.....	38
5.24 Improved model, (a) side view and (b) top view.....	38
6.1 Surface of the object from Marching cubes, (a) closed-up and (b) mesh representation.....	39
6.2 Metallic sphere, (a) actual model and (b) rendered model (Az. 0, El. 10, Tw. 0).....	41
6.3 Woodcarving, (a) actual model and (b) rendered model (Az. 15, El. 25, Tw. 0)	42
6.4 Foam cube, (a) actual model and (b) rendered model (Az.-40, El. 30, Tw. -20)	42
6.5 Ceramic cup, (a) actual model and (b) rendered model (Az. 70, El. 15, Tw. 10).....	42

This material is reserved for educational use only, not allowed for commercial use.

Figure	Page
6.6 Mannequin, (a) actual model and (b) rendered model (Az. -45, El. -25, Tw. 35)	43
6.7 Mannequin, (a) actual model and (b) rendered model (Az. 50, El. 15, Tw. 35)	43
6.8 Roman doll, (a) actual model and (b) rendered model (Az. -40, El. 20, Tw. -10)	44
6.9 Roman doll, (a) actual model and (b) rendered model (Az. 175, El. -15, Tw. 0).....	44
6.10 Hourglass, (a) actual model and (b) rendered model (Az. -20, El. 25, Tw. -10)	45
6.11 Foam head, (a) actual model and (b) rendered model (Az. 40, El. 30, Tw. 20)	45
6.12 Miniature truck, (a) actual model and (b) rendered model (Az. 120, El. -40, Tw. -30)	46
6.13 Measuring the area (volume) of the object by using cross products with each slice. The error occurring at the highlighted portion.....	47
A.1 Reconstruction of the color cross-section in an RGB mode.....	57
A.2 (a) original, (b) colorless, and (c) true-colored model (Az.170, El.-10, Tw.-5)	58
A.3 (a) original, (b) colorless, and (c) true-colored model (Az. 95, El.0, Tw. 0).....	58
A.4 (a) original, (b) rendered, and (c) true-colored model (Az.-10, El.10, Tw.-5)	58



Abbreviation

ART	Algebraic Reconstruction Technique
Az.	Azimuth Angle
BP	Backprojection
CG	Computer Generated, Computer Generation
CT	Computerized Tomography
El.	Elevation Angle
FBP	Filtered Backprojection
Fps.	Frames per Second
MBP	Modified Backprojection
MRI	Magnetic Resonance Imaging
MSE	Mean-Square Error
SART	Simultaneous Algebraic Reconstruction Technique
SIRT	Simultaneous Iterative Reconstruction Technique



Chapter 1

Introduction

1.1 Significance of the Problem

Shape extraction is the first step of many 3D applications, including 3D modeling, object recognition, robot navigation, machine inspection, geometry measurement, and so on. In order to satisfy these applications, the appropriate shape extraction methods are required.

1.2 Objective

In this research, the technique used to extract the shape from an object using tomography is investigated and extended to find the optimum condition of each parameter, to state and improve a flaw that might occur, and to demonstrate several precious applications. This technique, among those prior shape extraction techniques, is considered as one option, which may be proper for certain kinds of 3D applications.

1.3 Hypothesis

In the tomographic process, by directly replacing the projections of an object with the silhouetted photographs from sufficient viewpoints, one can acquire the pseudo cross-sections of an object, which means that only the outlines of the cross sections are correct, regardless of internal regions. Therefore, the *photographic tomography* could be inferred as one of the shape extraction techniques capable of reconstructing the volumetric data of an object from the sequence of photographs taken around the object.

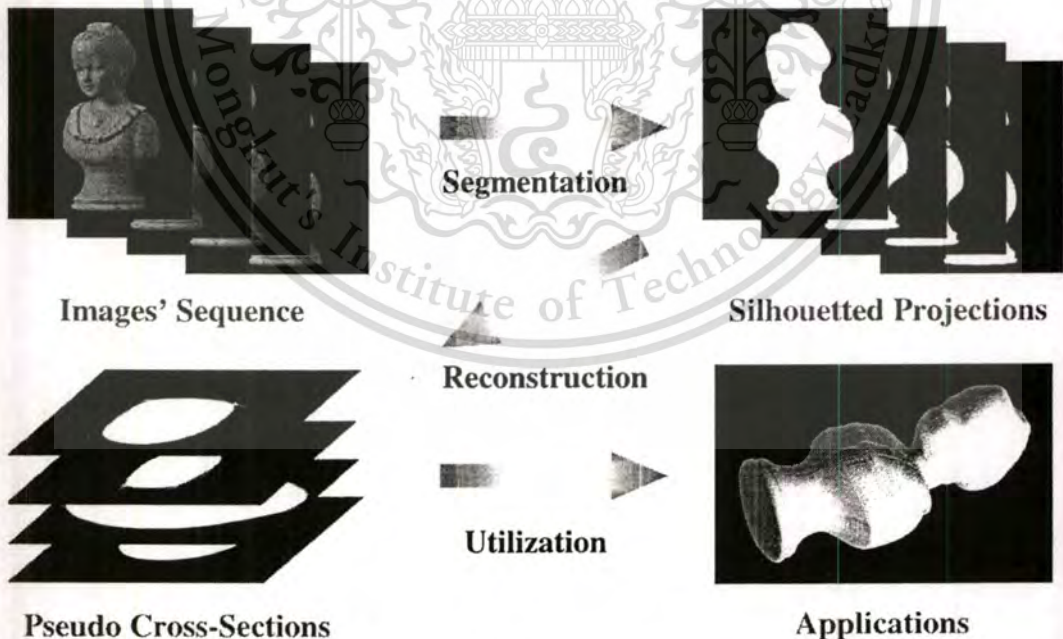


Fig. 1.1 The photographic tomography's process

1.4 Chapter Organizing

The succeeding chapters are fine organized as the following:-

Chapter 2 – Review of the related topics, the tomography and the shape extraction system

Chapter 3 – The principle of tomography including parallel backprojection, cone-beam backprojection, and algebraic reconstruction technique

Chapter 4 – Modified tomography for silhouetted projections, patch's occlusion problem, and archetype of imaging unit used in the research

Chapter 5 – The investigation to find the best parameter of the reconstruction, to verify the reconstruction, and to correct some errors

Chapter 6 – Demonstrations of some applications such as 3D modeling and geometric measurements

Chapter 7 – Conclusion and suggestion



Chapter 2

Tomography & Shape Extraction

Related to this research, the theories of tomography and shape extraction have been developed intensively and applied to numerous applications for an extended period of time. Their literatures which greatly influence on the fundamental understanding will be reviewed in this chapter. In addition, it includes the works of photographic tomography which is the combination of tomography and shape extraction.

2.1 Tomography – Concept and Applications

Named after the founder, the principle of tomography, so called the *Radon transform theorem*, was established by J. Radon [1] since 1917, and extended to complex fields by A. Kirillov [2]. Diverged from its first application, a radio astronomy [3], it has been prevalently applied to many branches of sciences and industries, for instance, a medical imaging [4], a seismic exploration [5], a nondestructive testing [6], and an industrial measurement [7]. Aim of these works is unanimous, to see through the object being inspected without any demolishing.

Fundamentally, tomographic imaging concerns with reconstructing the internal image of inspected object from either transmitted or reflected data, so-called projections. The projections are collected by illuminating the object from many directions with the coherent source and receiving the output by a corresponding array of detectors. The cross section has a set of 1D data as its projections, while the stack of cross sections or completed object has a set of 2D data as its projections. Different magnitudes of the projection at each array's position describe the internal characteristics of the object such as energy absorption, refractive index, density, or even electrical coefficient. By inversion of the problem, one can remap these values onto their original locations, and give the image of cross section as a function of inspected character.

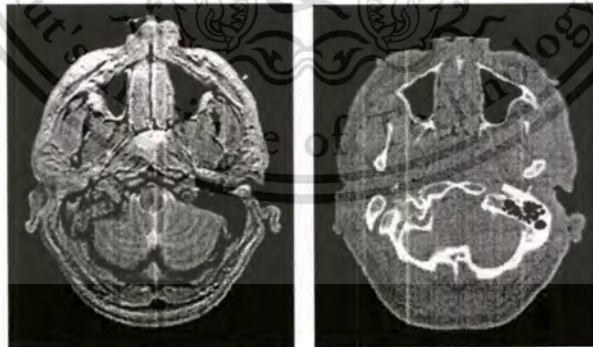


Fig. 2.1 Medical imaging – Cross sections of the human brain from MRI (left), and CT (right) [8]

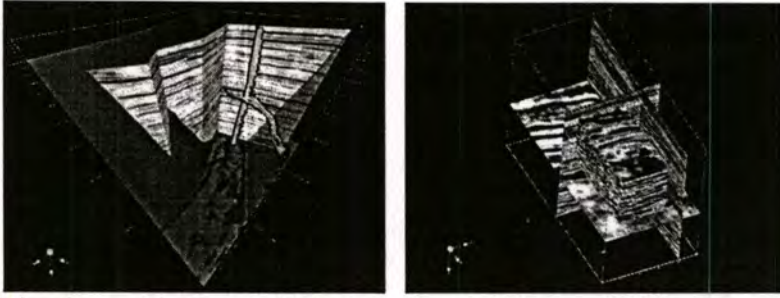


Fig. 2.2 Seismic exploration – Cutaway views of the earth [9]

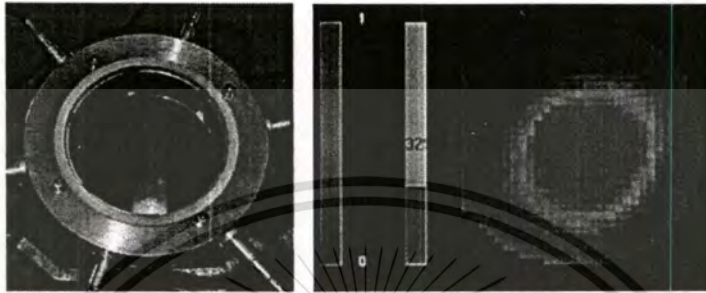


Fig. 2.3 Industrial measurement – Flame imaging using an electrical capacitance tomography [10]

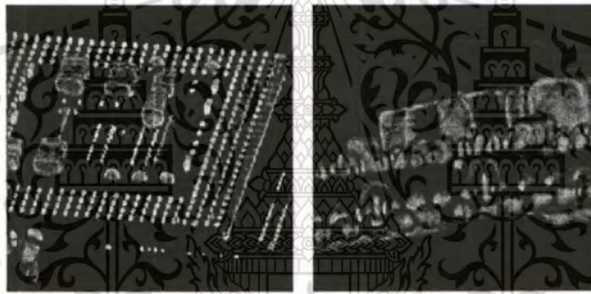


Fig. 2.4 Nondestructive testing – Tomographic image showing soldering irregularities inside the IC [11]

2.2 Shape Extraction Techniques

As stated before, when the tomographic process is applied to the object's photographs, only the contours of the object are achievable. Therefore, the process can be inferred as a 3D shape-extraction system, by which the shape of the object are probed and stored in some sorts of data for further utilization. Nowadays, several shape extraction systems are proposed, and each one is suitable in the limited range of applications. Some of those systems, including stereoscopy, laser range finder, structured-light projection, and shape from shading, will be reviewed here concisely.

The first 3D perception method, which was explored for a long time, is stereoscopy [12, 13]. Its concept is replicated from the human visual system by using two images from two different angles to perceive the depth of the scene. Practically, an orientation of each camera as well as a correspondent problem is elaborate, and the decision for the points of landmarks must be made manually.

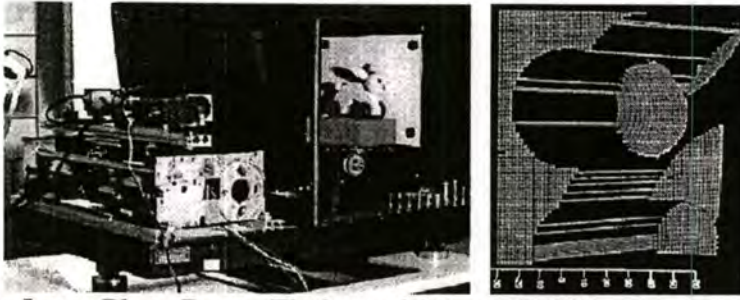


Fig. 2.5 The Laser Plane Range Finder and 3D result [15].

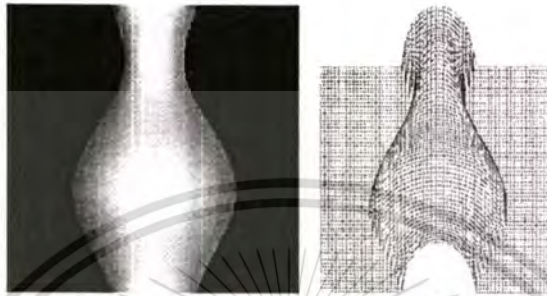


Fig. 2.6 Synthetic vase and its depth map using the shape from shading [18]

Laser range finder technique [14] straightforwardly measures the distances from the viewer to points on surfaces in the scene by using the time-of-flight of laser beams. Giving a high precision of a depth map, the “Laser Plane Range Finder” [15] is claimed about 0.5 mm in depth’s resolution. Commonly, the machine is fragile and costly.

Structured-light projection technique [16] projects some light patterns, for instance – plane or grid, onto a surface of the object, captures the scene, and then computes the shape from the distorted light. It has a main advantage that the discontinuity and monotony of the surface are abruptly replaced by the readily-computed artificial light pattern. This method, similar to the stereoscopy, suffers from the correspondent problem.

Shape from shading [17, 18] – the shape information could be inferred from only one monocular image if the illuminating position of light and the surface property of the object were known. However, the quality of result sensitively depends on the surface’s reflectance property. For some kinds of images, never does the shape from shading provide a correct solution [19].

All of the prior shape extraction techniques described above have different characteristics and satisfy different tasks. In the next section, the literatures of the tomographic process applied to photographs of the object, including its advantages and disadvantages, will be explained perspicuously.

2.3 Shape Extraction Using Photographic Tomography – The Reviews

The idea of shape from multiple views has come to an attraction since 1983 [20]. The multiple views may be referred to the silhouettes, called shape from silhouettes [21-25], or the grayscale or color images, called shape from photo-consistency [26-29]. Each algorithm has a different characteristic [30], but it can be classified into 2 major classes by geometric representation, the orthogonal view [21] and the perspective view [24]. (The orthogonal view and the perspective view are comparable to the parallel-beam and cone-beam projection respectively, both of which are

This material is reserved for educational use only, not allowed for commercial use.

explained in Chapter 3). These algorithms can be found in a number of applications such as the virtual reality [31] or the human motion modeling [32-33].

In 1999, the tomographic process is known to have the capability of giving the shape of an object from its photographs since the coincident experiments of D.T. Gering and W.M. Wells III [34] using parallel-beam tomography and A.J. Johnson and his colleagues [35] using cone-beam tomography. Afterwards, the work is extended many times [36-38]. Even though the lens-based camera is more preferable due to its convenience, there exist the usages of other camera systems such as pinhole camera [39], coherence imager [40], and cubic-phase-aberrated system [41].

The advantages of the shape extraction using photographic tomography are as the following:-

- Giving the full 3D shape of an object within an individual process with neither image registration nor other supplementary techniques.
- Disregarding to both material property and light position.
- Using locally available, less complicated, and affordable equipment.
- Working on a simple and well-developed reconstruction problem.
- Having an ability to adjust the accuracy, depending on the resolution of the photographs.

Nevertheless, the prerequisites of tomographic process applied to photographs for 3D shape extraction that should be denoted here are as follows:-

- The inspected object has a convex shape, or has no totally concave occlusion (See chapter 4).
- The center of rotation of the object (the object must be rotated around itself to take the photographs in different aspects) and the center of photographs are an identical line.
- For easily segregating the object from background, the color of background is recommended to be contrasting from the color of object.

Chapter 3

Tomographic Imaging for Non-Diffracting Source

Unless the rays of visible light pass through the object, the assumption of the non-diffracting source is valid because the refractive index of the traveling path is homogeneous. As a result, the conventional theorem for direct ray can be applied to the photographic tomography with a few changes (See chapter 4).

In this chapter, the introduction to the tomographic imaging for non-diffracting source, including a parallel-beam tomography, cone-beam tomography, and algebraic reconstruction technique, is described concisely.

3.1 Parallel-Beam Tomography

When array of sources and array of detectors are arranged correspondingly, the rays are considered as parallel beams since all the rays' paths are parallel to one another. This is the key property of the parallel-beam tomography, the theories of which include parallel-beam projection, Fourier slice theorem, and parallel-beam backprojection.

3.1.1 Parallel-Beam Projection

The parallel-beam projection, or the *Radon transform*, of function $f(x,y)$, denoted by $P_\theta(t)$, is defined as its line integral along the line AB, which makes perpendicular to another line inclined at angle θ from the x -axis, at the distance t from the origin. Practically, function $f(x, y)$ is the cross-sectional image and function $P_\theta(t)$ is the projection at specific angle.

If the rotated coordinates (t, s) from (x, y) with angle θ was given by

$$\begin{bmatrix} t \\ s \end{bmatrix} = \begin{bmatrix} \cos \theta & \sin \theta \\ -\sin \theta & \cos \theta \end{bmatrix} \begin{bmatrix} x \\ y \end{bmatrix} \quad (3.1)$$

the equation of line AB in Fig. 3.1 would be

$$x \cos \theta + y \sin \theta = t, \quad (3.2)$$

From Fig. 3.1, the projection of function $f(x, y)$ can be expressed by line integral as

$$P_\theta(t) = \int_{-\infty}^{\infty} f(t, s) ds \quad (3.3)$$

By changing coordinates to normal and using delta function, Eq. 3.3 is rewritten as

$$P_\theta(t) = \int_{-\infty}^{\infty} \int_{-\infty}^{\infty} f(x, y) \delta(x \cos \theta + y \sin \theta - t) dx dy \quad (3.4)$$

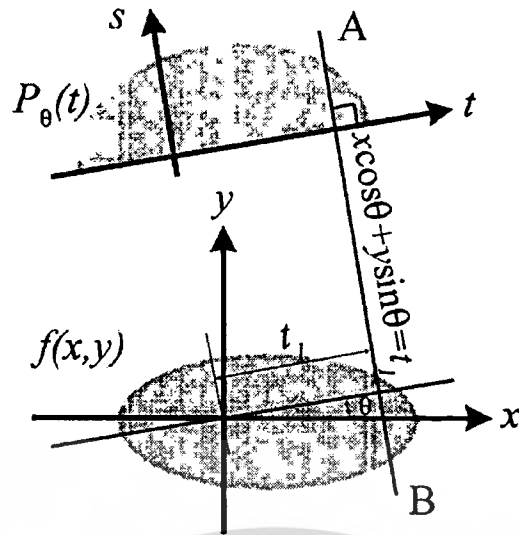


Fig. 3.1 Parallel-beam projection of function $f(x, y)$ at angle θ [42]

3.1.2 Fourier Slice Theorem [43]

Proving of the Fourier slice theorem relates one-dimensional Fourier transform of the projection to two-dimensional Fourier transform of the cross section. This relation is the principle which leads to the filtered-backprojection algorithm.

One-dimensional Fourier transform of the projection at angle θ is given by

$$S_{\theta}(\omega) = \int_{-\infty}^{\infty} P_{\theta}(t) e^{-j2\pi\omega t} dt \quad (3.5)$$

where ω is the frequency axis. Substituting Eq. 3.3 into Eq. 3.5 yields

$$S_{\theta}(\omega) = \int_{-\infty}^{\infty} \left[\int_{-\infty}^{\infty} f(t, s) ds \right] e^{-j2\pi\omega t} dt \quad (3.6)$$

Change the coordinates to (x, y) by using Eq. 3.3 and Eq. 3.4

$$S_{\theta}(\omega) = \int_{-\infty}^{\infty} \int_{-\infty}^{\infty} f(x, y) e^{-j2\pi\omega(x \cos \theta + y \sin \theta)} dx dy \quad (3.7)$$

Two-dimensional Fourier transform of the cross section is written as

$$F(u, v) = \int_{-\infty}^{\infty} \int_{-\infty}^{\infty} f(x, y) e^{-j2\pi(ux+vy)} dx dy \quad (3.8)$$

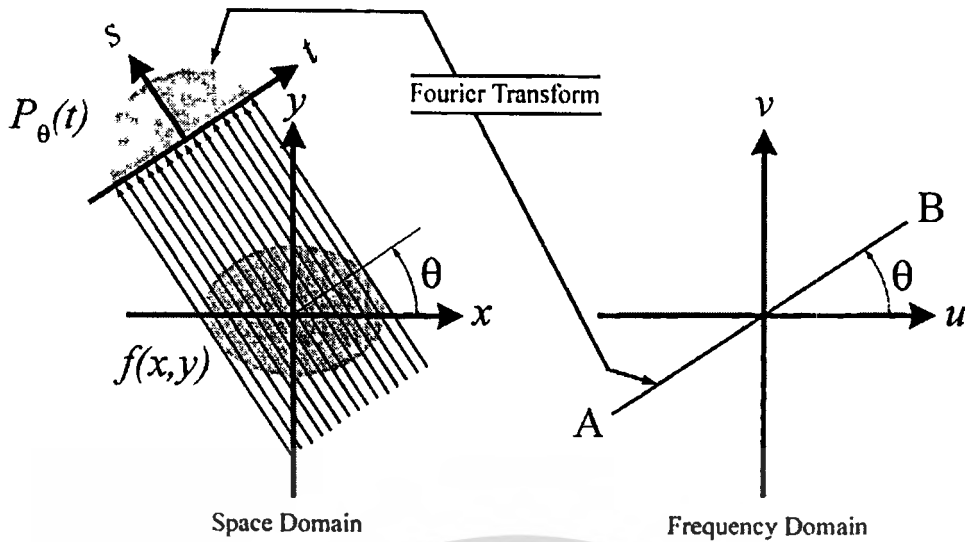


Fig. 3.2 The relationship between the projection of the object and the Fourier transform of the object function

From Eq. 3.7 and Eq. 3.8, it is obviously seen that the one-dimensional Fourier transform of the projection $S_\theta(\omega)$ is related to the two-dimensional Fourier transform of the cross section $F(u, v)$ when the polar coordinates (ω, θ) is changed to the Cartesian coordinates (u, v) , or

$$S_\theta(\omega) = F(\omega, \theta) = F(\omega \cos \theta, \omega \sin \theta) = F(u, v) \quad (3.9)$$

This relation is the Fourier slice theorem which is stated by [44] as the following

The Fourier transform of a parallel projection of an image $f(x, y)$ taken at angle θ gives a slice of the two-dimensional transform, $F(u, v)$, subtending an angle θ with the u -axis. In other words, the Fourier transform of $P_\theta(t)$ gives the value of $F(u, v)$ along line AB in Fig. 3.2.

3.1.3 Filtered-Backprojection Algorithm

From the Fourier slice theorem, the filtered-backprojection algorithm is derived to reconstruct the cross section from a series of projections. Practically, the backprojection can be thought as smearing all the filtered projections across a 2D-plane.

Two-dimensional inverse Fourier transform of the $F(u, v)$ is given by

$$f(x, y) = \int_{-\infty}^{\infty} \int_{-\infty}^{\infty} F(u, v) e^{j2\pi(ux+vy)} du dv \quad (3.10)$$

Change from the Cartesian coordinates (u, v) to the polar coordinates (ω, θ) by using

$$\begin{aligned} u &= \omega \cos \theta \\ v &= \omega \sin \theta \end{aligned} \quad (3.11)$$

$$du dv = \omega d\omega d\theta$$

This material is reserved for educational use only, not allowed for commercial use.

Forbidden to modify the content, and cite the document when use.

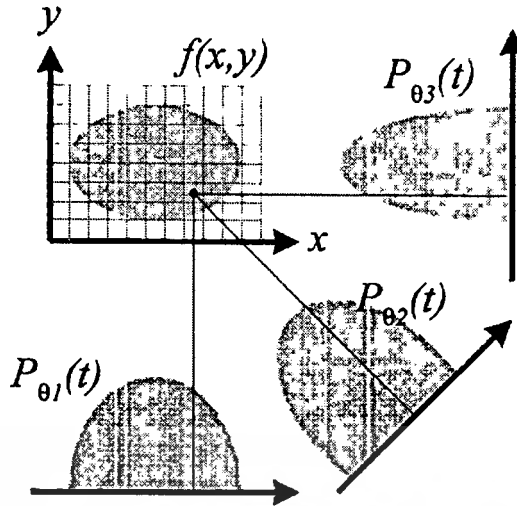


Fig. 3.3 The concept of reconstruction by backprojection

From Eq. 3.10 and Eq 3.11

$$f(x, y) = \int_0^{2\pi} \int_0^{\infty} F(\omega, \theta) e^{j2\pi\omega(x \cos \theta + y \sin \theta)} \omega d\omega d\theta \quad (3.12)$$

Expand the outermost integration to two parts, from 0 to π and from π to 2π

$$f(x, y) = \int_0^{\pi} \int_0^{\infty} F(\omega, \theta) e^{j2\pi\omega(x \cos \theta + y \sin \theta)} \omega d\omega d\theta + \int_0^{\pi} \int_0^{\infty} F(\omega, \theta + 180^\circ) e^{j2\pi\omega[x \cos(\theta + 180^\circ) + y \sin(\theta + 180^\circ)]} \omega d\omega d\theta \quad (3.13)$$

Using this property

$$F(\omega, \theta + 180^\circ) = F(-\omega, \theta) \quad (3.14)$$

Eq. 3.13 can be rewritten as

$$f(x, y) = \int_0^{\pi} \int_{-\infty}^{\infty} F(\omega, \theta) e^{j2\pi\omega} |\omega| d\omega d\theta \quad (3.15)$$

From the Fourier slice theorem in Eq. 3.9, the projections are related with the cross section by this expression

$$f(x, y) = \int_0^{\pi} \int_{-\infty}^{\infty} S_{\theta}(\omega) |\omega| e^{j2\pi\omega} d\omega d\theta \quad (3.16)$$

The equation above is the filtered-backprojection algorithm, in which $|\omega|$ is the ramp filter and $S_\theta(\omega)$ is the Fourier transformation of the projection $P_\theta(t)$. The algorithm can be separated into two steps, the backprojection and the filtration, or

$$f(x, y) = \int_0^\pi Q_\theta(x \cos \theta + y \sin \theta) d\theta \quad (3.17)$$

$$Q_\theta(t) = \int_{-\infty}^{\infty} S_\theta(\omega) |\omega| e^{j2\pi\omega t} d\omega \quad (3.18)$$

3.2 Cone-beam Tomography

Differing from parallel-beam tomography, cone-beam tomography has a point source confronted with a two-dimensional array of detectors; therefore, the rays' paths form the conical shape. The parallel-beam algorithm could be implemented in this situation if and only if the distance between source and the detector approached to infinity; otherwise, it must be replaced by the cone-beam algorithm.

3.2.1 Cone-Beam Projection

In three-dimensional volume, the rotated coordinates (t, s, r) from (x, y, z) with the azimuth angle θ and the elevation angle γ is written in a matrix form as

$$\begin{bmatrix} t \\ s \\ r \end{bmatrix} = \begin{bmatrix} 1 & 0 & 0 \\ 0 & \cos \gamma & \sin \gamma \\ 0 & -\sin \gamma & \cos \gamma \end{bmatrix} \begin{bmatrix} \cos \theta & \sin \theta & 0 \\ -\sin \theta & \cos \theta & 0 \\ 0 & 0 & 1 \end{bmatrix} \begin{bmatrix} x \\ y \\ z \end{bmatrix} \quad (3.19)$$

The projection at coordinates (t, r) is the intersection of two planes, which are

$$t = x \cos \theta + y \sin \theta \quad (3.20)$$

$$r = -(-x \sin \theta + y \cos \theta) \sin \gamma + z \cos \gamma \quad (3.21)$$

Hence, the three-dimensional *parallel projection* is given by

$$P_{\theta, \gamma}(t, r) = \int_{-s_m}^{s_m} f(t, s, r) ds \quad (3.22)$$

By changing the coordinates to normal and using the delta function with Eq. 3.20 and Eq. 3.21, the projection is rewritten as

$$P_{\theta, \gamma}(t, r) = \iiint_{vol} dx dy dz f(x, y, z) \delta(x \cos \theta + y \sin \theta - t) \\ \times \delta(-(-x \sin \theta + y \cos \theta) \sin \gamma + z \cos \gamma - r) \quad (3.23)$$

From the equation, the projection ray is specified by 4 variables, (t, θ) in the horizontal plane, and (r, γ) in the vertical plane.

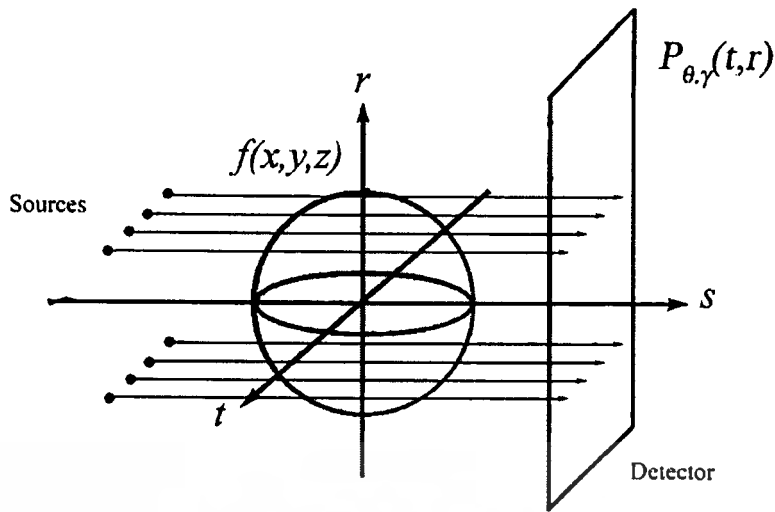


Fig. 3.4 3D parallel-beam geometry

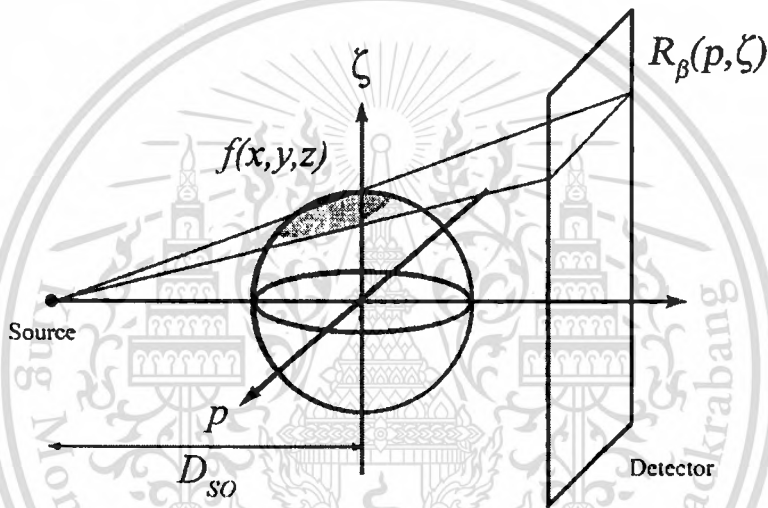


Fig. 3.5 Cone-beam geometry

For the given cone-beam projection $R_{\beta}(p, \zeta)$ where β is a rotating angle and (p, ζ) are coordinates on the detector plane, the equivalent parallel ray can be found from

$$R_{\beta}(p, \zeta) = P_{\theta, \gamma}(t, r) \quad (3.24)$$

The parallel variables (t, θ) and (r, γ) is calculated from

$$t = p \frac{D_{SO}}{\sqrt{D_{SO}^2 + p^2}} \quad (3.25)$$

$$\theta = \beta + \arctan(p / D_{SO})$$

$$r = \zeta \frac{D_{SO}}{\sqrt{D_{SO}^2 + \zeta^2}} \quad (3.26)$$

$$\gamma = \arctan(\zeta / D_{SO})$$

where D_{SO} is the distance from the center of rotation to source.

This material is reserved for educational use only, not allowed for commercial use.

- Forbidden to modify the content, and cite the document when use.

3.2.2 Cone-Beam Backprojection

Based on Felkamp's cone-beam algorithm [45], the cone-beam backprojection is derived from the tilted fan-beam geometry on the basis of the filtered backprojection algorithm. Only the formula is described here regardless of the proof.

The three-dimensional function $f(x, y, z)$ is related to the two-dimensional projection $R_\beta(p, \zeta)$ by the following equation

$$f(x, y, z) = \frac{1}{2} \int_0^{2\pi} \frac{D_{so}^2}{(D_{so} - s)^2} \int_{-\infty}^{\infty} R_\beta(p, \zeta) h\left(\frac{D_{so}t}{D_{so} - s} - p\right) \frac{D_{so}}{\sqrt{D_{so}^2 + \zeta^2 + p^2}} dp d\beta \quad (3.27)$$

The reconstruction can be simplified by separation into 3 steps, weighting, convolving, and backprojecting.

- Weighting the projection data

$$R'_\beta(p, \zeta) = \frac{D_{so}}{\sqrt{D_{so}^2 + \zeta^2 + p^2}} R_\beta(p, \zeta) \quad (3.28)$$

- Convoluting the weighted projection data with the filter kernel

$$Q_\beta(p, \zeta) = R'_\beta(p, \zeta) * h(p) \quad (3.29)$$

- Backprojecting to obtain the three-dimensional function

$$f(x, y, z) = \frac{1}{2} \int_0^{2\pi} \frac{D_{so}^2}{(D_{so} - s)^2} Q_\beta\left(\frac{D_{so}t}{D_{so} - s}, \frac{D_{so}z}{D_{so} - s}\right) d\beta \quad (3.30)$$

3.3 Algebraic Formulation

The algebraic formulations such as the Algebraic Reconstruction Technique (ART) [46], the Simultaneous Iterative Reconstruction Technique (SIRT) [47], and the Simultaneous Algebraic Reconstruction Technique (SART) [48] can reconstruct the cross section with different approach from the filtered-backprojection technique. The cross section is regarded as a group of unknown variables with the underdetermined condition from the projections, and can be solved by using the numerical procedures. This method has the flexibility to reconstruct the tomographic image in the presence of limited projection [49], but it has a foible on the time consumption due to the iteration. It is noted that the study of this research is limited to the ART.

The projection equation of the ART can be expressed as the following

$$p_i = \sum_{j=1}^N w_{ij} f_j \quad , i = 1, 2, \dots, M \quad (3.31)$$

Here, f_j is the value of reconstruction grid element, p_i is the value of the i^{th} projection point or ray sum, the weight factor w_{ij} is the fraction area of the j^{th} image cell intercepted by the i^{th} ray, N is the number of pixels, and M is the number of projection points.

This material is reserved for educational use only, not allowed for commercial use.

Forbidden to modify the content, and cite the document when use.

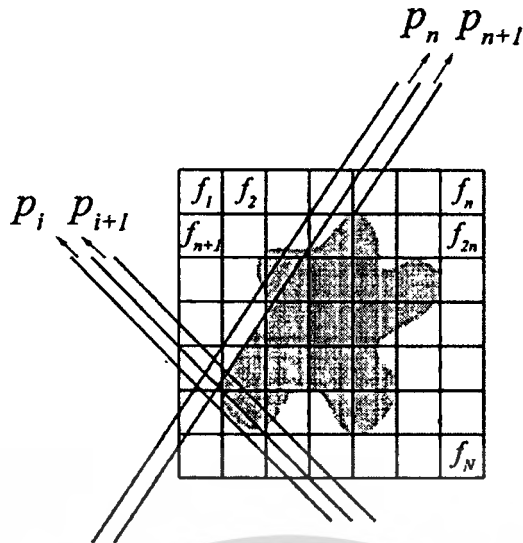


Fig. 3.6 Algebraic Reconstruction Technique, each cell representing an unknown variable in the linear equations

For the large and unequal M and N , the conventional inversion of metric to find the solution to the problem is not an option. A numerical procedure is introduced to search an answer repetitively. First, the initial conjectures, $f_j^{(0)}$, are made for the solution. By substituting them in Eq. 3.32 and Eq. 3.33, more improved result could be obtainable. When this process is done repeatedly until the certain point, the solution will be nearby the real answer.

$$f_j^{(i)} = f_j^{(i-1)} + \frac{p_i - q_i}{\sum_{k=1}^N w_{ik}^2} \cdot w_{ij} \quad (3.32)$$

$$q_i = \sum_{k=1}^N f_k^{(i-1)} w_{ik} \quad (3.33)$$

Chapter 4

Modified Tomography for Silhouetted Projections

The entire process of modified tomography applied to the silhouetted projections is elucidated in this chapter. It starts with how the camera system is related to the cone-beam projection and how the pseudo cross-sections are obtained from the series of photographs, followed by the problem of patch's occlusion and classification of the problem. In the end, the device used to help record the photographs around the object will be discussed thoroughly.

4.1 Modified Tomography

In order to modify the tomographic algorithm to have a capability of extracting shape from photographs of the object, it is required that the relation between the camera system and the projection be substantiated. This requirement is about to be fulfilled in the subsequent section. Consequently, the modification of tomography can be done unambiguously.

4.1.1 Camera System and Cone-Beam Projection

Normally, projections are gathered from radiation of specific frequency of ray through the object, and each projection can be described mathematically by the function of integration as explained in the preceding chapter. For the shape extraction purpose, the projections are absolutely different because they are the photographic images which are taken from scene radiation of the opaque object rather than having the ray penetrate the object. However, both types of projections have a common character since the ray, whether it is the visible light or not, travels directly in the homogeneous substance.

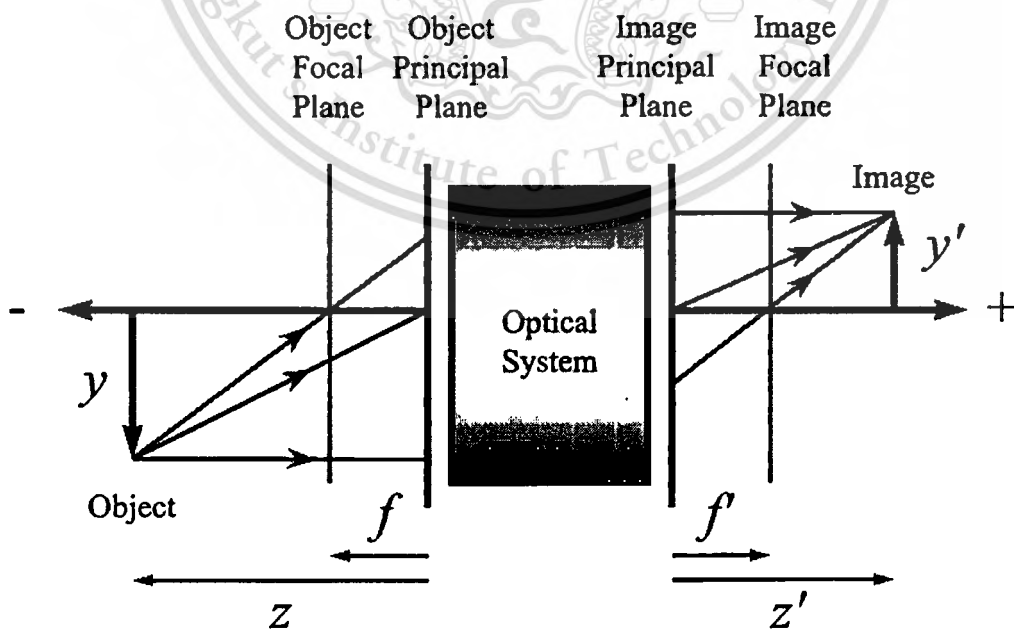


Fig. 4.1 The ordinary optical system [36]

(Paraphrased from [36]) In Fig. 4.1, if the object is laid in the depth-of-field i.e. in focus, Newton's lens equation [50] relate the image y' to the object y as

$$\frac{y'}{y} = -\frac{f}{z-f} = -\frac{z'-f'}{f'} \quad (4.1)$$

where f and f' are the object's and optical focal length, also z and z' are distances of object and image from the principal planes respectively. Eq. 4.1 can be rearranged to

$$\frac{y'}{z'} = -\left(\frac{f}{f'}\right)\frac{y}{z} \quad (4.2)$$

or the slope of the image space subtended to the optical axis is proportion to the slope of the object space subtended to the object axis. Each sensor located on the image plane can be considered to measure the power from all the sources along the same slope y/z , which is a projection of the source that intersects the center of both principle plane. The projections form a cone so the image plane measures the cone-beam projection. As a result, the distance of the cone D_{SO} is the distance between the image sensor and the image principal plane, or equal to z' .

4.1.2 Modified Reconstruction Algorithm

The relation between the camera system and cone-beam geometry has been proved apparently in the previous section. Hence, the backprojection algorithm can be occupied with a few alterations to conform to the silhouetted projections. On account of [34], it is advised that filtering by the ramp function in the algorithm is unnecessary for this type of projection. Accordingly, the equation for the parallel-beam algorithm is rewritten as

$$f(x, y) = \int_0^\pi P'_\theta(x \cos \theta + y \sin \theta) d\theta \quad (4.3)$$

where $f(x, y)$ is the cross-sectional function, $P'_\theta(t)$ is the one-dimensional silhouetted projection, and θ is the rotational angle.

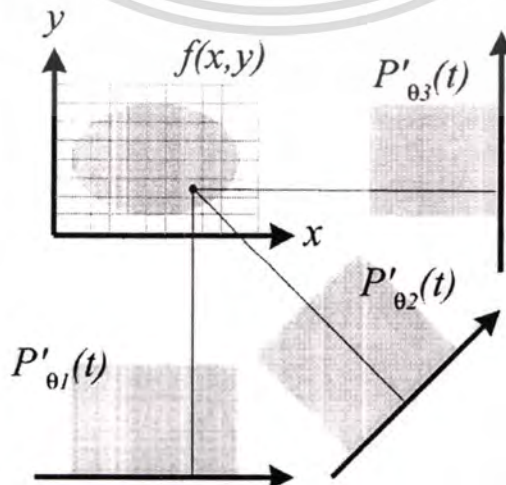


Fig. 4.2 Parallel-beam backprojection of silhouetted projections

This material is reserved for educational use only, not allowed for commercial use.

Forbidden to modify the content, and cite the document when use.

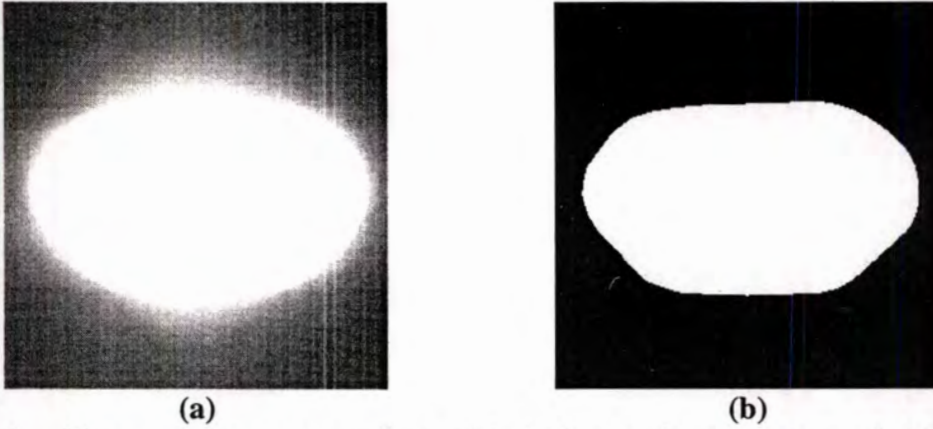


Fig. 4.3 The pseudo cross-sections, (a) before enhancement, and (b) after enhancement

The cone-beam algorithm is rewritten as

$$f(x, y, z) = \frac{1}{2} \int_0^{2\pi} \frac{D_{SO}^2}{(D_{SO} - s)^2} R_{\beta} \left(\frac{D_{SO}t}{D_{SO} - s}, \frac{D_{SO}z}{D_{SO} - s} \right) d\beta \quad (4.4)$$

where $f(x, y, z)$ is the volumetric data, $R_{\beta}(p, \zeta)$ is the two-dimensional silhouetted projection, β is the rotational angle, D_{SO} is the cone distance, and (t, s) are the coordinates which are rotated from (x, y) .

After the reconstruction, the pseudo cross-section whose internal detail is not real is available. The sample of pseudo cross-section is demonstrated in Fig 4.3(a). The boundary of the shape is vague because of the star artifacts [51] in the background. This problem can be eliminated by using image enhancement, the straightforward way of which is thresholding with the maximum value because the area that contains this value is the intersecting area of all the projections. The cross section which is already enhanced is shown in Fig. 4.3(b).

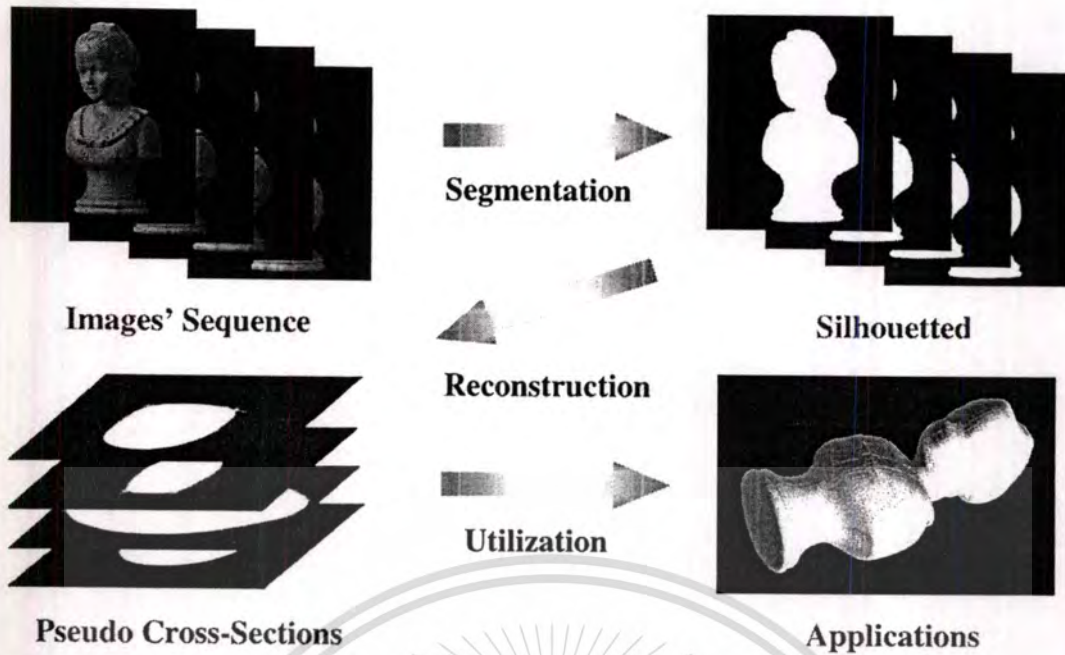


Fig. 4.4 The process diagram of the photographic tomography

4.1.3 Shape Extraction Process

The entire process for the shape extraction from a series of photographs is shown as a diagram in Fig. 4.4. This process starts with capturing a number of images around the inspected object, which will be elaborated in section of imaging unit. As stated before, the method concerns only the shape or outline of the object; therefore, the segmentation procedure, the thresholding for high-contrasting image or the blue-screen technique for the others, is brought up to turn the captured images into binary format where the background is equal to zero and the foreground is equal to one. As a result, this kind of shape extraction algorithm can extract the shape of any object regardless of the type of surface either the Lambertian or non-Lambertian surface. When the binary images or the silhouetted projections are passed into the modified reconstruction algorithm described previously, the stack of enhanced pseudo cross-sections whose shape is comparable to its original is attainable. This stack of cross sections can be utilized in such applications as a 3D shape modeling, geometric measurement, and so on.

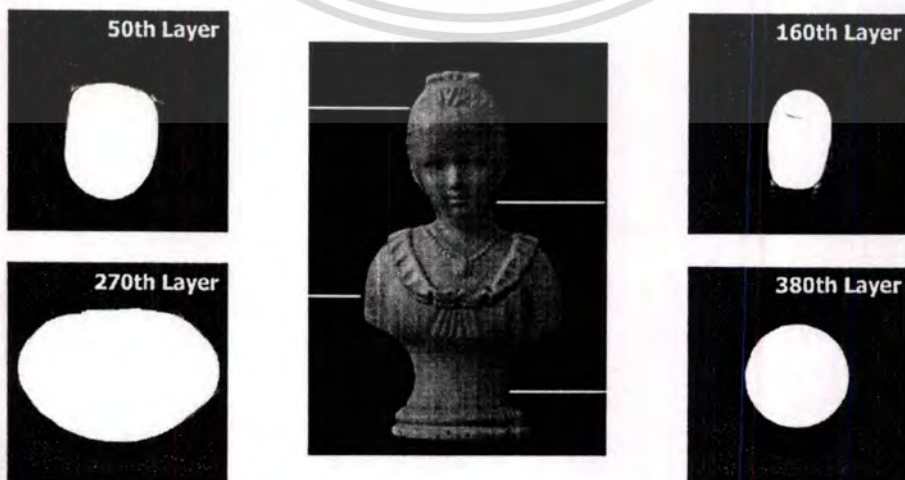


Fig. 4.5 Examples of pseudo cross sections

This material is reserved for educational use only, not allowed for commercial use.

Forbidden to modify the content, and cite the document when use.

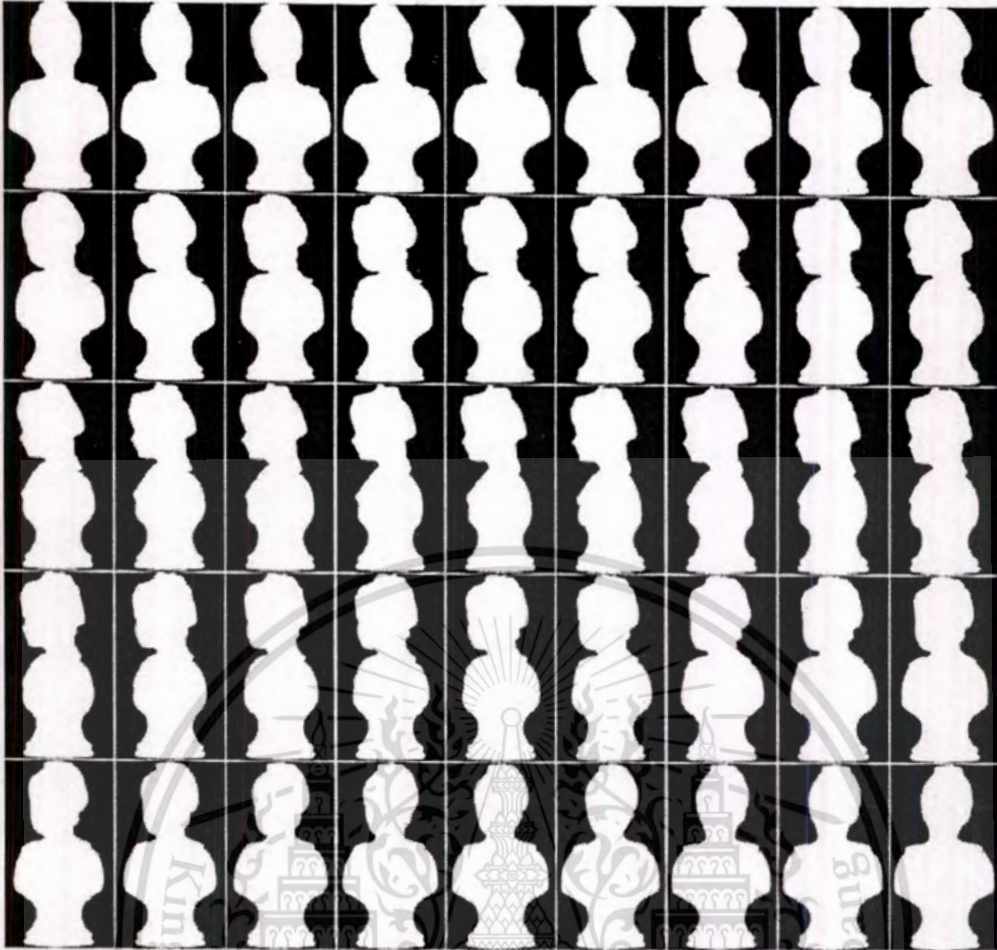


Fig. 4.6 The montage of silhouetted projections in the half plane

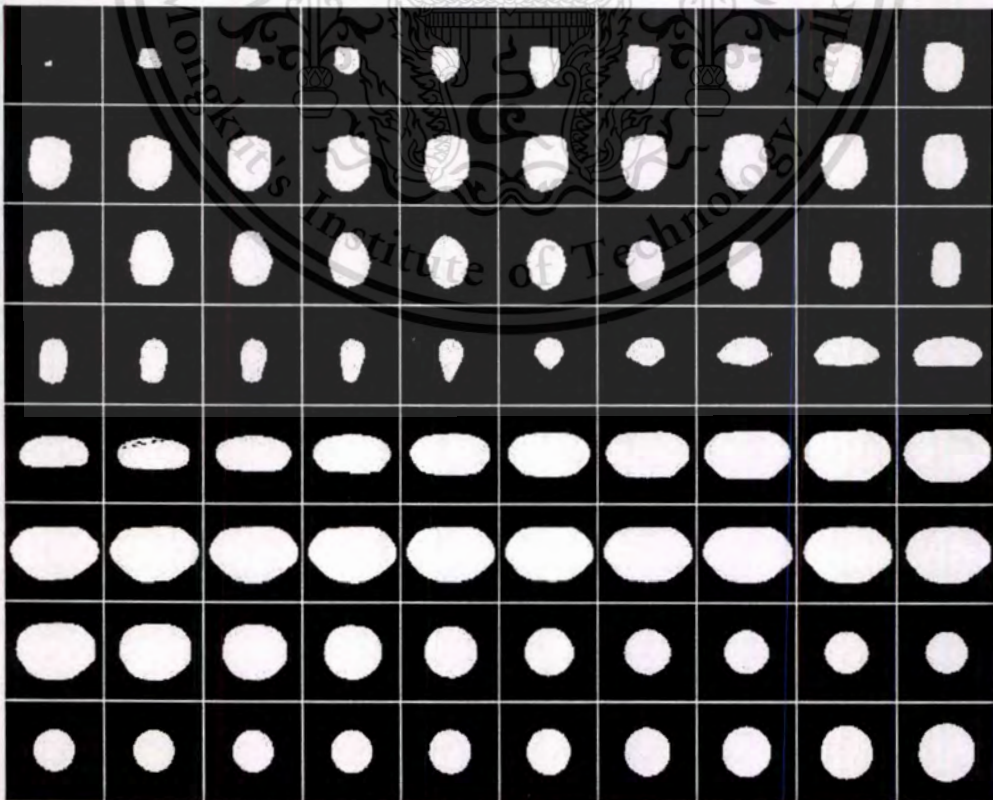


Fig. 4.7 The montage of pseudo cross sections displayed at every 5 layers

This material is reserved for educational use only, not allowed for commercial use.

Forbidden to modify the content, and cite the document when use.

4.2 Patch's Occlusion

In the silhouetted projection, patch's occlusion always occurs and makes the reconstructed cross section not identical to its origin. The occluded patch doesn't mean only the patch which is blinded from the viewer by other parts of object, but it also means the patch which can be seen from the viewer but never lies on the edge of projections. *Therefore, the occluded patch is defined as the patch that doesn't contribute itself to the outline of any silhouetted projection, whether it can be seen from the viewer or not.* The occlusion may be classified into two categories, the concave occlusion and the perspective occlusion, as the following:-

4.2.1 Concave Occlusion

On reconstructing the cross section from its silhouetted projections, a major problem arises when the investigated object has a concave shape, the area where is curved inward, since the silhouettes never give adequate detail about that. In Fig. 4.8 are shown the samples of cross sections that give the same shape after they are reconstructed.

In the case of three dimensions, the concave occlusion may be further divided into two types, a partially-concave occlusion and a totally-concave occlusion. The partial occlusion exists in some rotational axes while the total occlusion exists in all rotational axes. As shown in Fig. 4.9(a), the partial occlusion exists along z axis of the model. Therefore, the reconstructed model from a series of projections rotated about this axis possibly gets error. In order to avoid the problem, one might make projections regarding to another axis. This is not true for the total occlusion shown in Fig. 4.9(b). Even though the object is rotated regarding any axis, the reconstruction encounters with the erroneous result.

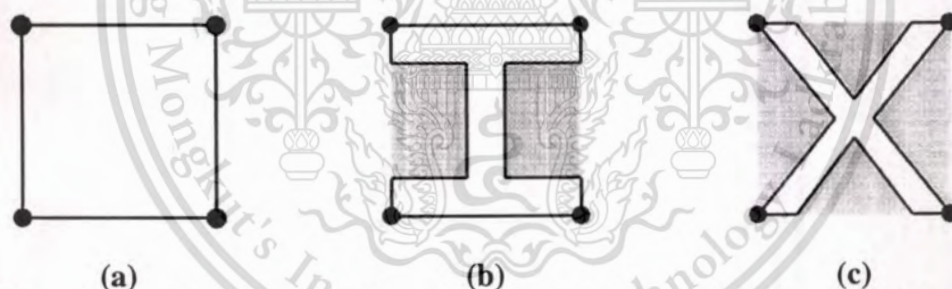


Fig. 4.8 Three cross-sections giving the same reconstructed image [36]. The shaded zones are the occluded area, and the solid dots are the dominating points.

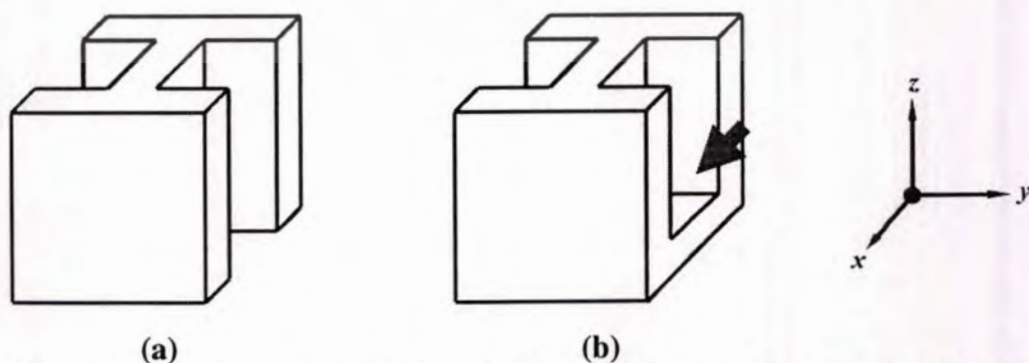


Fig. 4.9 Cubes showing two types of occlusions, (a) partially-concave occlusion and (b) totally-concave occlusion. The marker indicating the totally-occluded area

This material is reserved for educational use only, not allowed for commercial use.

Forbidden to modify the content, and cite the document when use.

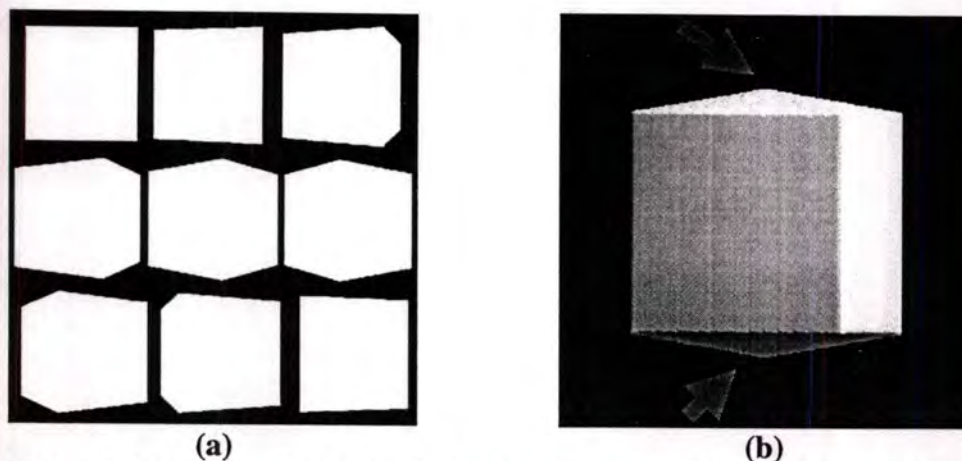


Fig. 4.10 (a) 2D perspective projections at the distance of $2x$ from the center of cube and (b) the erroneously reconstructed cube because of the occlusion on the top and bottom (Az. -15 , El. 0)

4.2.2 Perspective Occlusion

Perspective occlusion problem always occurs in the top and bottom area of the model when the distance between detector and object is too short. For example, when someone is standing in front of the building, he or she cannot see details lying on the roof. This is the case happening in the imaging system as well. Fig. 4.10 shows the set of perspective projections and the erroneously reconstructed cube when the eye position is very close to the cube. The solution to this problem is somewhat straightforward. By pulling the eye position far away from the object, patches on the top and bottom could be seen clearly as the outline of the projections.

4.3 Imaging Unit

In order to collect a series of photographs from the inspected object, it is suggested to rotate the object about the origin i.e. its axis and take the photograph using a fixed camera rather than to move the camera around the vertex path. This idea is substantial for the object which is motionless and small to medium-sized, the common characters of most of the objects. By adhering to this idea, the imaging unit can be assembled simply from a few components, and less in complexity.

The imaging unit shown in Fig. 4.11 is mainly composed of a digital camera and an controllable rotating platform. The camera is placed in the position at one end of the rail pointing directly to the platform. The rotating platform is installed on dual rails where it can be moved toward the camera. As a result, the distance between the camera and object placed on the platform is adjustable. Controlled by a computer, the rotating platform is capable of rotating precisely to any specified angle, while the digital camera used to record the images of rotated object is also connected to and controlled by the same computer. For simply extracting the silhouette from the photograph, the object is placed in front of the background contrasting from the color of object, and illuminated by an ambient light to avoid specula artifacts.

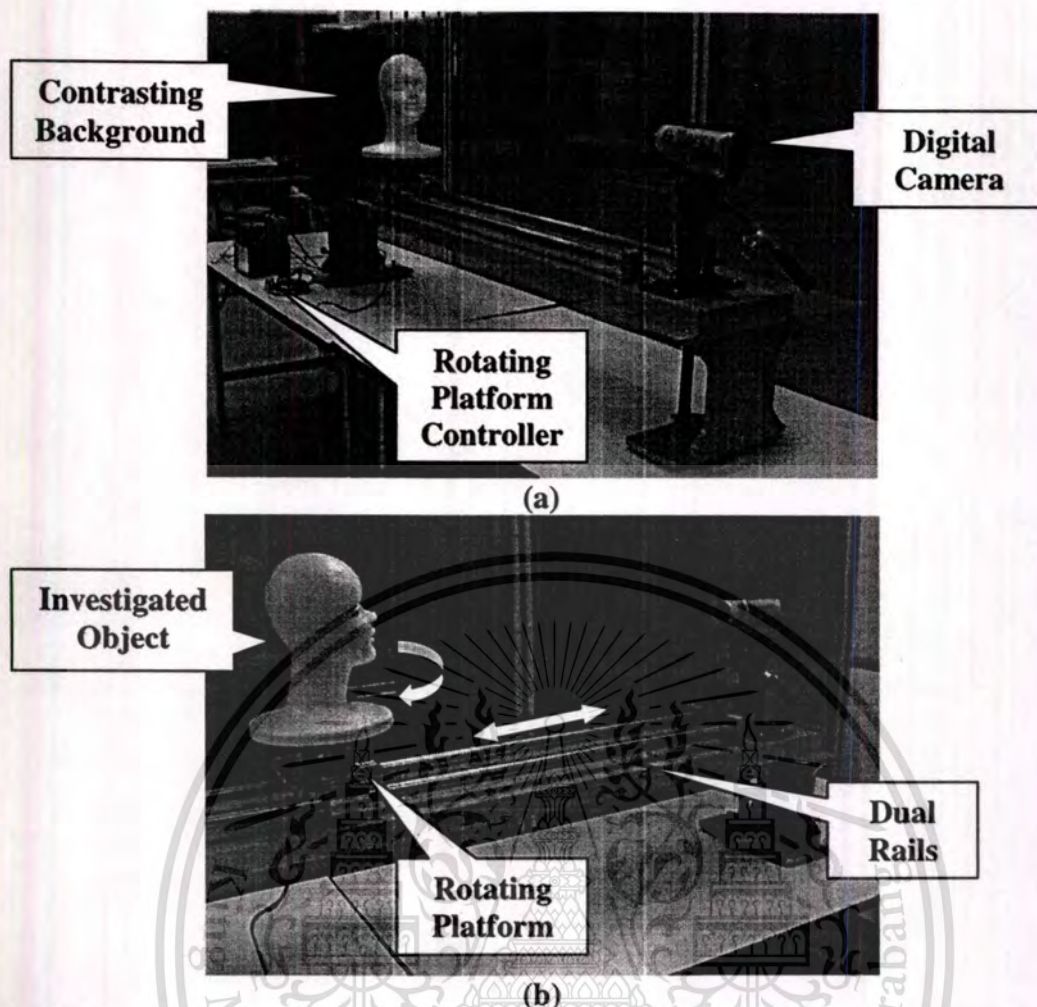


Fig. 4.11 The prototype of an imaging unit for acquiring the sequence of photographs consisting of digital camera and rotating platform placed on dual rails.

The unit has a capability of capturing the photograph of the object in two modes, a still-photo capturing and a movie capturing. The still-photo capturing mode is done straightforwardly by repeatedly rotating the object to a specified angle and taking a photograph of the object at the current view. For the parallel-beam geometry, only the half plane or 180 degrees of projections is required because of the symmetry of the object's outlines.

In the movie capturing mode, it is recommended that the camera record a movie from two full turns around the object to avoid the problem of unstable speed at start and stop of the rotating platform. A series of one full-turn images of the object is then extracted from the middle portion of the recorded movie, whereas the new arbitrary starting and stopping points are indicated from the two most matching frames. The degree of rotation per single frame is explicitly calculated from Eq. 4.4.

$$\text{Angle/Frame} = \frac{360^\circ}{\text{fps} \times T} \quad (4.5)$$

where fps is a frame rate, and T is a time to complete one full turn in second.

Chapter 5

Evaluation of the Reconstruction

In this chapter, the computer simulation along with the real implementation plays an important role to evaluate the reconstruction topology. Choosing optimum conditions for the reconstruction is a decision-concerned process to find a high quality cross-sectional image while maintain time consumption. By doing the simulations with computer-generated models, one can obtain precise results under controlled environments, and these results can be used to make the decisions for the conditions. After the simulations, qualified conditions are confirmed by performing the practical implementation on an object and estimating the error from the reproduction procedure. In the end of this chapter, an improving scheme for partially-concave occlusions along multiple axes is demonstrated by means of simulation.

5.1 Optimum Conditions of the Reconstructions

The main conditions which have to be considered consist of the reconstruction technique, whether it should be the Filtered Backprojection (FBP), the Modified Backprojection (MBP), or the Algebraic Reconstruction Technique (ART), the number of projections, and the reconstruction geometry. As stated above, the correctness and the swiftness of the topology are taken into account to find the most reasonable conditions by measuring the mean-square error (MSE) of grayscale of the cross section and the time consumption of the process, respectively. Hence, to ensure the precision of the results, all of the experiments in this section are accomplished by doing the simulation with the CG (Computer Generated) datasets. A set of 2D models or cross sections is used to simulate for the first 2 factors, the reconstruction technique and the number of projections, while a set of 3D models is used to simulate for the reconstruction geometry.

The mean-square error in percentage is directly calculated from

$$MSE(\%) = \frac{\iint [o(\vec{r}) - o'(\vec{r})]^2 d\vec{r}}{\iint [o(\vec{r})]^2 d\vec{r}} \times 100 \quad (5.1)$$

where $o(r)$ is the grayscale of original model, $o'(r)$ is the grayscale of reconstructed model, and r is the region of interest. It is noted that the specification of testing computer is as the following: 1.33GHz AMD Athlon processor, 512 Mbytes SDRAM, and C++ simulating program running on Windows XP operating system.

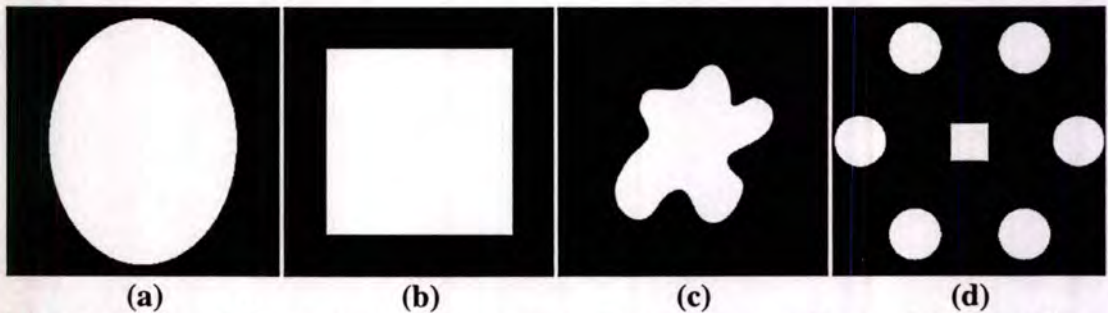


Fig. 5.1 The CG cross sections representing various patterns, (a) the ellipse, (b) the rectangle, (c) the blob, and (d) the multi-circles

This material is reserved for educational use only, not allowed for commercial use.

Forbidden to modify the content, and cite the document when use.

5.1.1 Reconstruction Technique

Three techniques from two classes of the reconstruction algorithms discussed in Chapter 3 will be manipulated to reconstruct the pseudo cross-section from its series of silhouetted parallel-beam projections. Those techniques consist of the conventional filtered-backprojection, the algebraic reconstruction technique, and the modified backprojection which is the backprojection without filtering, followed by binarizing the output image. The cross-sectional set to be tested in Fig. 5.1 is selected carefully to make them have distinct characteristics from one another. The ellipse represents a typical convex-shape model; the rectangle represents a sharp corner model; the blob represents a concave-occlusion model; the multi-circles represents a complicated model. All of the models are sized 256 by 256 pixels. The simulation is done by taking the parallel projections of these cross sections in 90 angles around the half, binarizing them to create the pattern of inverse-silhouetted photograph, and then reconstructing the cross sections by 3 techniques. The MSE values and average time usages are shown in Table 5.1, while the reconstructed cross section are shown in Fig. 5.2 through 5.5.

By considering the reconstructed set of ellipses, every technique gives correct boundaries excepting the MBP which gives the filled shape leading to the lowest MSE. For a sharp-corner model like the rectangle, the FBP and the ART totally fail to give a clear-cut boundary while the MBP preserves its correctness. Representing the concave occlusion, the blob cannot be reconstructed correctly by any technique because the occluded patches do not express themselves on outlines of all projections. For the multi-circle case, the MBP gives the best result among 3 techniques with some error due to unseen patches. The MBP not only gives the best results, but it also uses the shortest time to complete the reconstruction. Conspicuously, the MBP is the superlative choice to reconstruct a cross section from its silhouetted projections with a high quality as well as low time consumption. For these reasons, this technique will be employed in all of the experimentations from now on. It is noted that in the successive iterations the ART does not give any improvement.

Table 5.1 MSE and time usage of the reconstructed cross sections by different reconstruction techniques*

Cross Section	Reconstruction Technique		
	FBP** (%)	MBP (%)	ART*** (%)
Ellipse	79.379	1.117	66.376
Rectangle	92.924	1.609	82.732
Blob	84.730	27.244	68.159
Multi-Circles	74.967	9.516	56.861
Averg. Time Usage (sec.)	1.583	1.529	3.458

* 90 projections in a half plane, linear interpolation

** Hann windows, normalized cutoff frequency 0.8

*** First Iteration

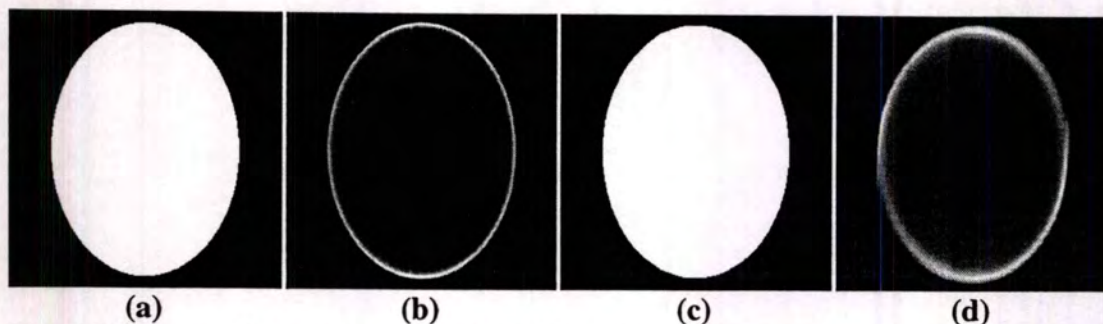


Fig. 5.2 The ellipses reconstructed by each technique, (a) prototype, (b) FBP, (c) MBP, and (d) ART

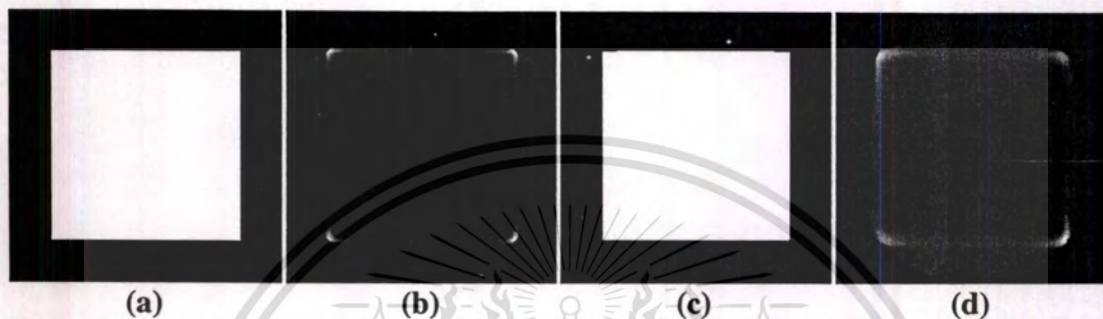


Fig. 5.3 The rectangles reconstructed by each technique, (a) prototype, (b) FBP, (c) MBP, and (d) ART

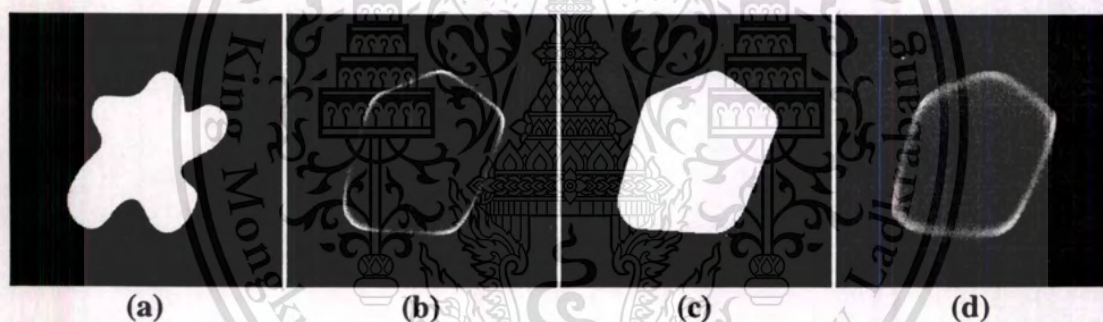


Fig. 5.4 The blobs reconstructed by each technique, (a) prototype, (b) FBP, (c) MBP, and (d) ART

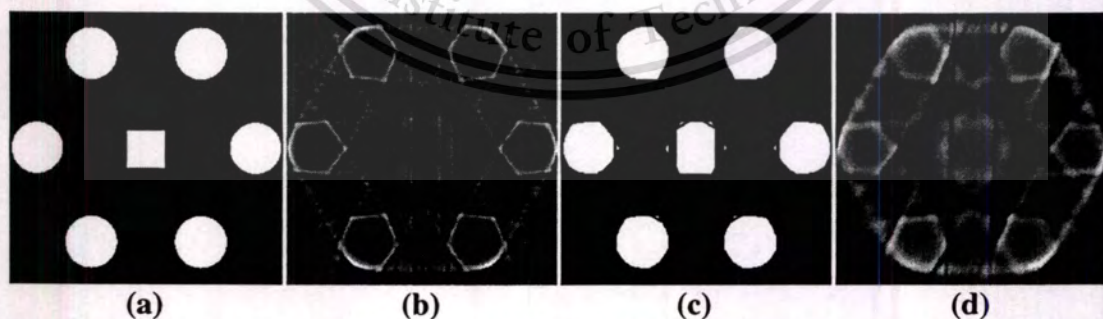
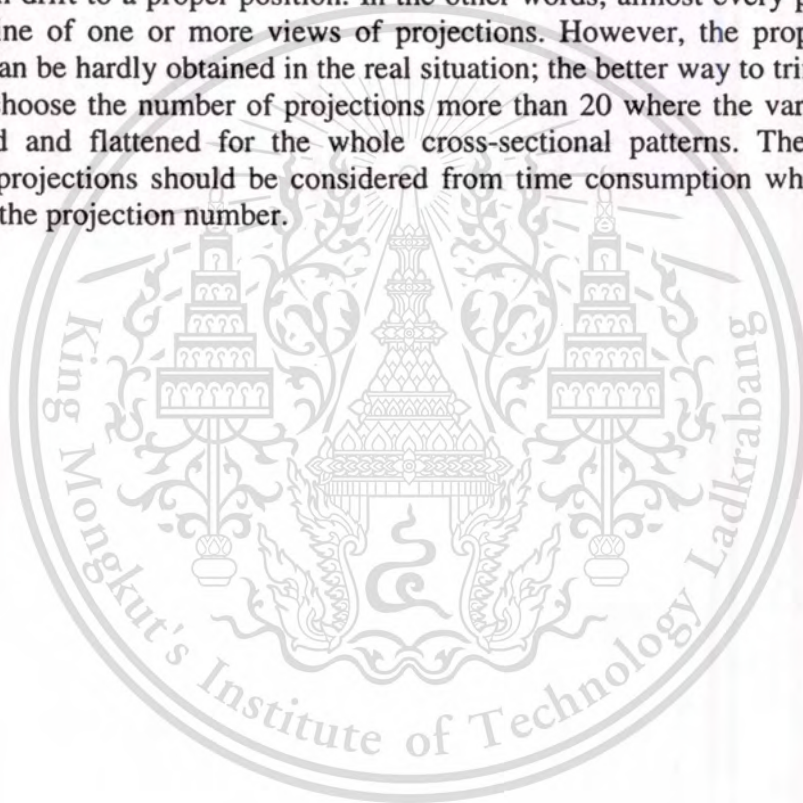


Fig. 5.5 The multi-circles reconstructed by each technique, (a) prototype, (b) FBP, (c) MBP, and (d) ART

5.1.2 Number of Projections

In order to determine the appropriate number of projections for the reconstruction, the set of cross sections in Fig. 5.1 is reclaimed in this situation with variations of the projection numbers selected from integers between 1 and 180. The MSE together with the time usage is recorded and graphed in Table 5.2 and Fig. 5.10, respectively; also some of the reconstructed cross sections are demonstrated progressively in Fig. 5.6 to 5.9.

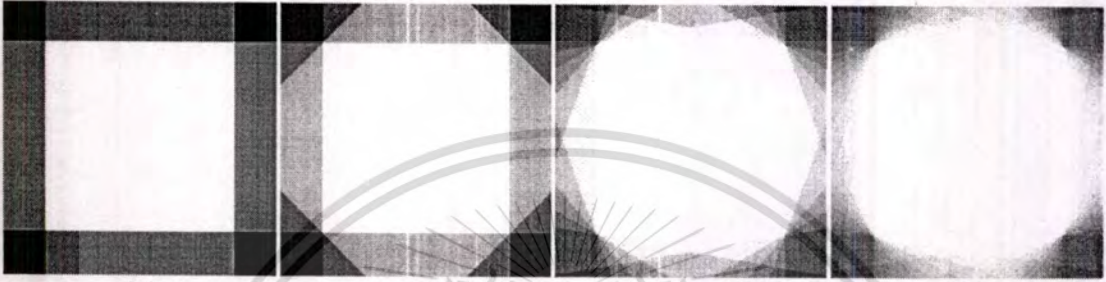
From the graph, the errors of the ellipse and the blob normally decay when the number of projections increases. On the other hand, the errors of the rectangle and the multi-circles unsteadily decay depending on *views of projection*. What makes the errors unsteady could be described perspicuously from Fig. 5.19, the case of the multi-circles. When the projections is 5, the error is about 125%; after adding a single projection, the error drops dramatically to 12%, and increases again to 81% for 9 projections. The fast dropping of the error occurs because the addition makes a sight of projection drift to a proper position. In the other words, almost every patch is laid on the outline of one or more views of projections. However, the proper sight of projection can be hardly obtained in the real situation; the better way to trim down the error is to choose the number of projections more than 20 where the variation is by now stabled and flattened for the whole cross-sectional patterns. The maximum number of projections should be considered from time consumption which linearly depends on the projection number.





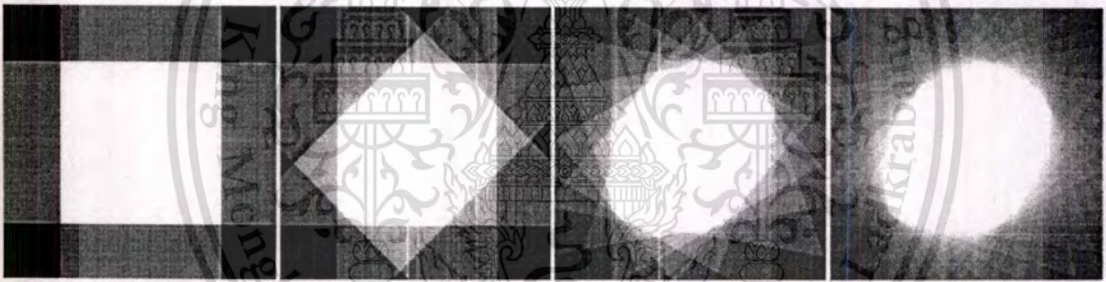
(a) (b) (c) (d)

Fig. 5.6 The ellipses reconstructed from different numbers of projections (without threshold), (a) 2, (b) 4, (c) 9, and (d) 20



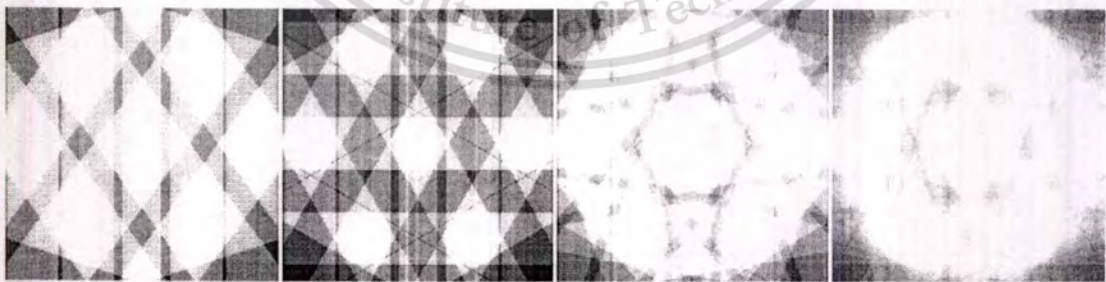
(a) (b) (c) (d)

Fig. 5.7 The rectangles reconstructed from different numbers of projections (without threshold), (a) 2, (b) 4, (c) 9, and (d) 20



(a) (b) (c) (d)

Fig. 5.8 The blobs reconstructed from different numbers of projections (without threshold), (a) 2, (b) 4, (c) 9, and (d) 20



(a) (b) (c) (d)

Fig. 5.9 The multi-circles reconstructed from different numbers of projections (without threshold), (a) 5, (b) 6, (c) 9, and (d) 20. A rapid dropping of the error occurring in (b)

Table 5.2 MSE and time usage of the reconstructed cross-sections with different numbers of projections by the MBP*

Cross Section	Number of Projections											
	1	2	3	4	5	6	9	10	12			
Ellipse	39.010	27.187	12.008	6.689	4.878	3.601	2.431	1.931	1.839			
Rectangle	44.633	1.698	27.473	1.698	16.231	1.692	9.365	1.679	1.679			
Blob	193.447	73.669	55.355	45.596	42.916	37.695	34.147	31.190	31.670			
Multi-Circles	376.032	173.399	280.994	111.122	124.958	11.830	81.525	33.189	11.830			
Time (sec.)	0.020	0.040	0.060	0.070	0.080	0.100	0.150	0.170	0.201			

Table 5.2 (continue)

Cross Section	Number of Projections											
	15	18	20	30	36	45	60	90	180			
Ellipse	1.731	1.651	1.499	1.308	1.391	1.253	1.268	1.117	1.176			
Rectangle	5.062	1.685	1.666	1.653	1.673	2.285	1.634	1.609	1.503			
Blob	31.193	31.002	29.873	29.133	28.519	28.076	27.736	27.244	26.382			
Multi-Circles	23.382	10.349	15.065	9.831	10.203	13.552	9.629	9.516	9.305			
Time (sec.)	0.240	0.301	0.351	0.521	0.591	0.751	0.991	1.523	2.964			

* Half-plane projection, linear interpolation

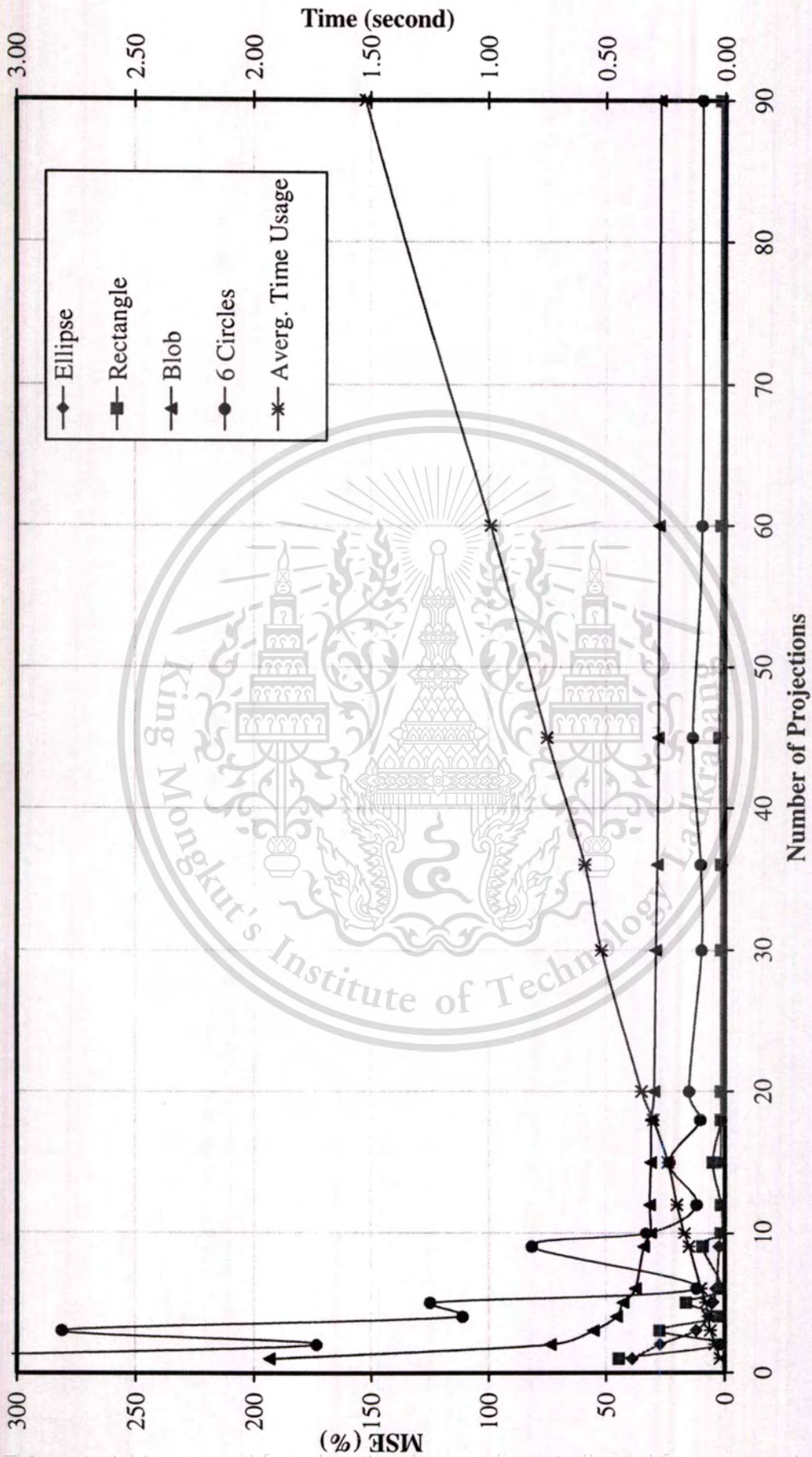


Fig. 5.10 Plotting of the MSE and time usage against the number of projections for all of the cross sections

This material is reserved for educational use only, not allowed for commercial use.

Forbidden to modify the content, and cite the document when use.

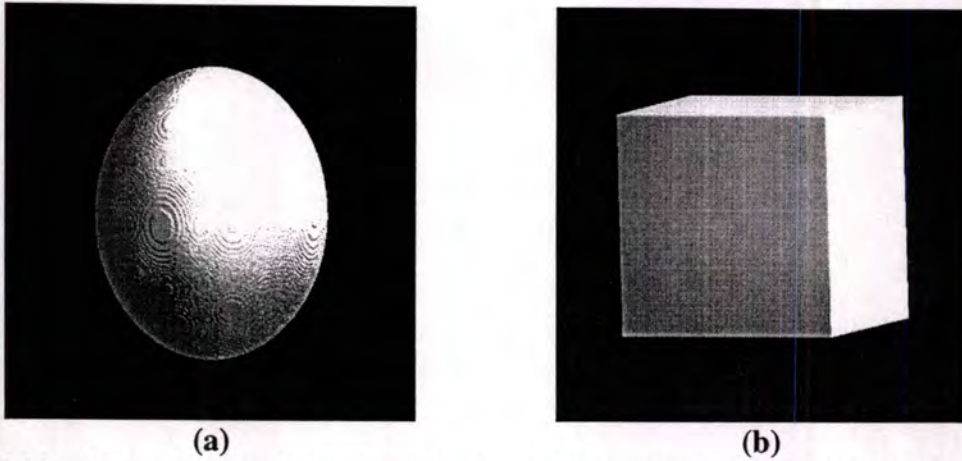


Fig. 5.11 3D models used to simulate the reconstruction geometry, (a) the ellipse (Az. -20, El. -5), (b) the cube (Az. -25, El. -5)

5.1.3 Reconstruction Geometry

It is two problems that should be taken into account for reconstructing a 3D model. One is a time consumption to treat an entire volume of the model, and the other is a *perspective occlusion problem* (see Chapter 4). The time consumption of the cone-beam backprojection algorithm is far greater than that of the parallel-beam backprojection algorithm because of a geometric difficulty.

In spite of the fact that a photograph is constructed from the cone-beam geometry, the geometry could be assumed as an orthogonal geometry if the position of the object were far enough from the focal plane. When this assumption is accepted, together the time consumption and the perspective occlusion problems of the cone-beam algorithm will be resolved apparently by using the parallel-beam algorithm as an alternative. To determine how far the distance of projection can be admitted as a parallel beam, two simple models shown in Fig. 5.11 are projected at a number of distances and reconstructed by both parallel and cone-beam algorithm. The results of MSE are recorded in Table 5.3, and some reconstructed models are demonstrated in Fig. 5.12. Noted that the volume sizes are 256×256×256 voxels.

Table 5.3 MSE of the reconstructed models with different distances of projections*

Model	Algorithm	Relative Distance**				
		2×	4×	8×	16×	∞***
Ellipse	Parallel	4.454	2.794	2.104	1.870	1.113
	Cone	1.909	1.958	1.991	2.137	2.449
Cube	Parallel	22.927	11.547	6.820	3.289	0.184
	Cone	7.792	4.168	4.209	2.874	2.252

* 72 projections in a full plane, nearest-neighbor interpolation

** Relative distance compared to the maximum thickness of the model

*** Infinity length for the cone-beam geometry set to 3,900× (999,999 pixels)

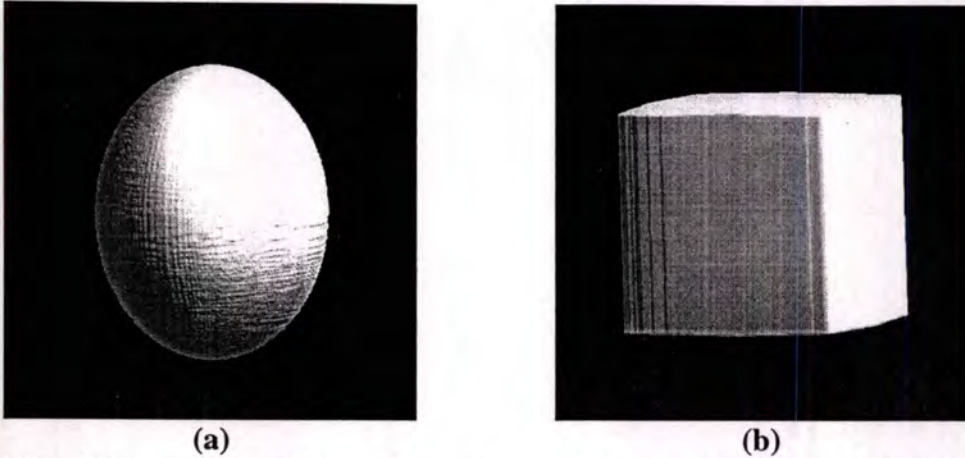


Fig. 5.12 3D reconstructed models at a distance of $16\times$ (a) the ellipse (Az. -20 , El. -5), (b) the cube (Az. -25 , El. -5)

From the simulation, the reconstruction processes of the parallel-beam algorithm and cone-beam algorithm take the average time of 38.636 seconds and 204.773 seconds, respectively. As a result, the processing time of the parallel-beam algorithm is 5 times lower than of the cone-beam algorithm. Moreover, the processing time of the parallel beam can be further reduced since only the half set of projections is required. Obviously, the parallel-beam algorithm has shown the superior to the cone-beam in the computational standpoint.

While the distance of projection approaches the infinity, the errors of both models reconstructed by the parallel-beam algorithm approach zero. For the cone-beam algorithm, the error should be consistent because the geometry is exactly matched, but the results in Table 5.3 do not agree with this phase. The gradual increase of the error in the case of the ellipse is mainly due to a rough of an interpolation method, while the abrupt decrease of the error in the case of the cube is due to the perspective occlusion problem in the very first distance. From the result, in order to use the parallel-beam algorithm with projections from a camera system, it is suggested that an investigated model be positioned faraway from the focal plane more than $16\times$ or 16 times the thickness of the model.

Up until now, the optimum conditions for reconstructing a 3D model have been clearly approved. Those three qualified conditions will be repeated here succinctly. First of all is the reconstruction technique, the modified backprojection giving the best result among three techniques within the shortest time. Second is the number of projections which should be in excess of 20 for the half plane, or the angle interval between two projections should be equal to or less than 9 degrees in other words. Additionally, the term, the more projections the reconstruction, the better quality the cross section, is not valid in this circumstance. The last is the reconstruction geometry; the parallel-backprojection algorithm could be applied if the distance between the model and camera were greater than 16 times of the model's thickness.

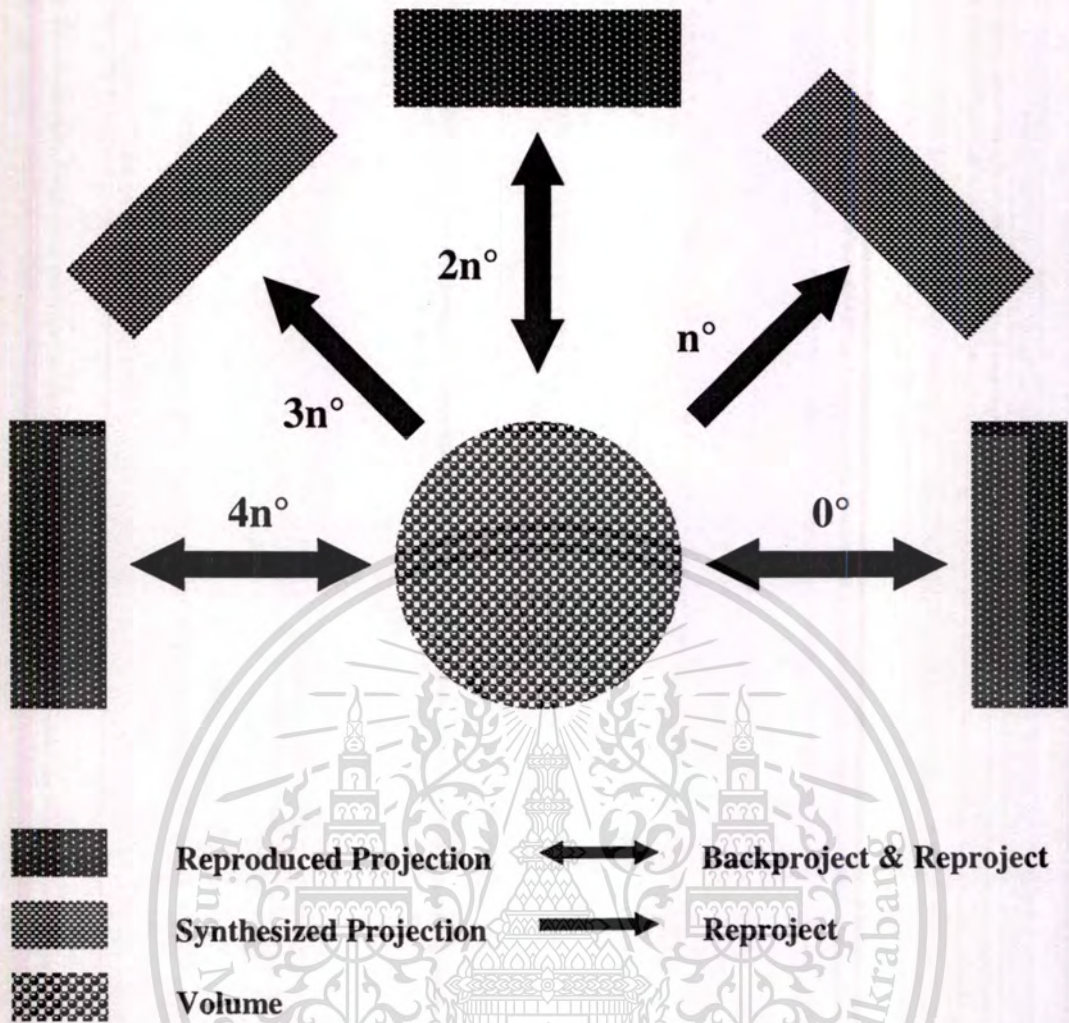


Fig. 5.13 Reprojection strategy

5.2 Practical Implementation

In order to substantiate the optimum conditions in the preceding section, the practical implementation is ended up with the reprojection strategy. Because the exact volumetric data of the real object is hard to be achieved, the error of reconstruction cannot directly be evaluated from point-to-point comparison. It is suggested to reproject the reconstructed volume onto the 2D plane in many viewpoints, and compare with the on-hand data. The reprojection process provides two types of projections, a reproduced projection if the viewpoint were the same as what is used in the reconstruction, and a synthesized projection if the viewpoint were another. Fig. 5.13 explains this process graphically. The conditions were acceptable if and only if the synthesized projections were correct.

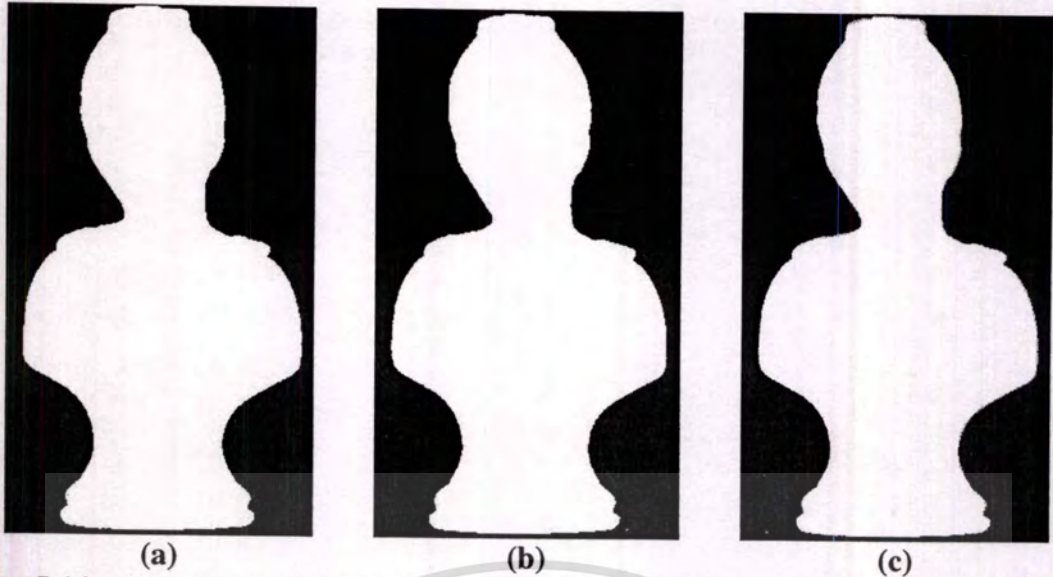


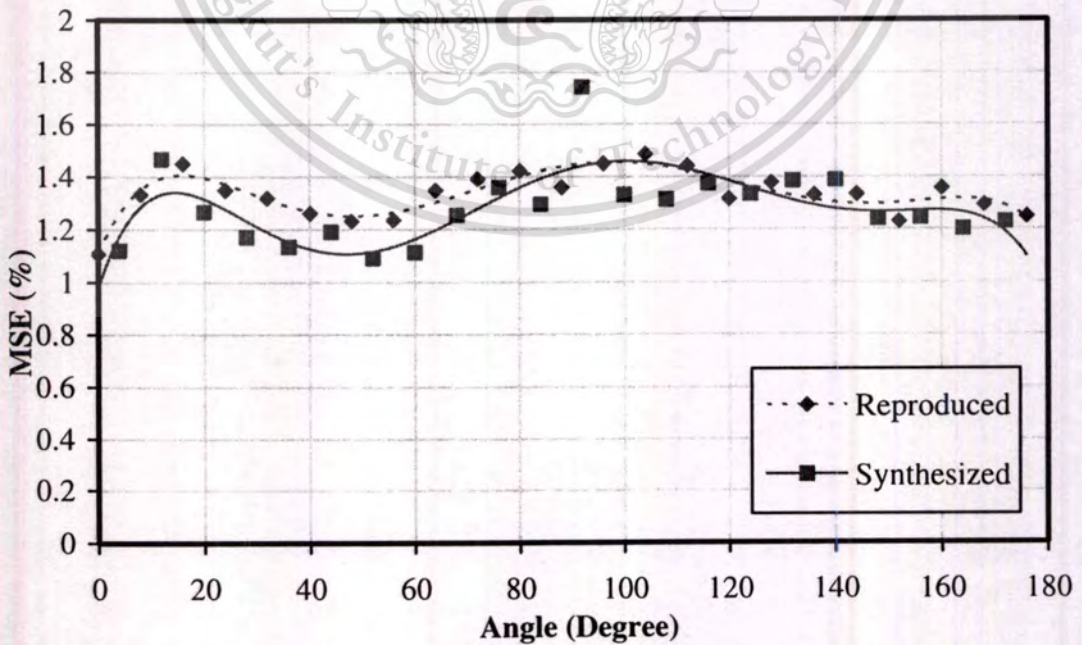
Fig. 5.14 Comparing of the synthesized projection to the original projection of the mannequin at degree 4, (a) original, (b) synthesized, and (c) synthesized pasted over original

Placed at a distance of $32\times$ from the focal plane, the mannequin (image in Chapter 6) is shot at every 4 degrees around the half, so there are 45 projections ready to be backprojected. However, only 23 projections selected from every other photograph are used, and the remainders are kept for a testing purpose. After the reconstruction which takes the time of 147.312 seconds using linear interpolation, the volume, having the dimension of $256\times 256\times 436$ voxels, is reprojected at every 4 degrees to make the projections resemble and comparable to the originals, giving both the reproduced and synthesized projections. The synthesized projection along with its corresponding real projection is demonstrated in Fig. 5.14, and the MSE of the imitated projections are tabled and graphed in Table 5.4 and Fig. 5.15, respectively.

It is undoubtedly seen from the results that either the reproduced or the synthesized projections have the tolerably low MSE value at all of the angles. However, these can partially confirm the optimum conditions because of the inadequate viewing direction.

Table. 5.4 MSE of the reproduced (normal) and synthesized (*italic*) projections

Angle (degree)	MSE (%)	Angle (degree)	MSE (%)	Angle (degree)	MSE (%)
0	1.106	64	1.348	128	1.377
4	<i>1.120</i>	68	<i>1.254</i>	132	<i>1.384</i>
8	1.333	72	1.392	136	1.330
12	<i>1.467</i>	76	<i>1.359</i>	140	<i>1.387</i>
16	1.449	80	1.422	144	1.332
20	<i>1.266</i>	84	<i>1.294</i>	148	<i>1.240</i>
24	1.349	88	1.359	152	1.228
28	<i>1.171</i>	92	<i>1.742</i>	156	<i>1.243</i>
32	1.318	96	1.449	160	1.356
36	<i>1.134</i>	100	<i>1.330</i>	164	<i>1.200</i>
40	1.262	104	1.485	168	1.292
44	<i>1.191</i>	108	<i>1.312</i>	172	<i>1.228</i>
48	1.232	112	1.440	176	1.247
52	<i>1.090</i>	116	<i>1.373</i>		
56	1.235	120	1.315		
60	<i>1.113</i>	124	<i>1.334</i>		

**Fig. 5.15** Plotting of MSE of reproduced and synthesized projections against angle of projections (the data are fitted by 6th order polynomial)

This material is reserved for educational use only, not allowed for commercial use.

Forbidden to modify the content, and cite the document when use.

5.3 Improving Scheme for Concave Object

When the object being investigated has a partially concave occlusion along more than one axis like the excavated cube in Fig. 5.16(a), rotating the object with respect to single axis cannot completely divulge the occluded patches hidden along other axes. In order to improve the model, it is suggested to have two reconstructed models, both of which are reconstructed with respect to different axis so that these two models are the complement for each other, and the finalized model is the intersection of them. To corroborate and clarify this idea, the simulation as well as the implementation is set up in the succeeding subsections.

5.3.1 Simulation

Three different models have been prepared for the simulation process with diverse characteristics. Made from CG, the holed cube and the jointed tori have characters of partially concave occlusion while the third model modified from the volumetric data of the CT-scanned teapot [52] has a character of both partially- and totally-concave occlusion. All of the models rendered in Fig. 5.16 are sized of $256 \times 256 \times 256$ voxels.

In the simulation, the model is rotated about the origin with respect to each axis and projected onto a 2D plane, and then reconstructed by the MBP. In order to reduce the error from the occlusion, the models reconstructed from different axes of rotation are intersected, giving an improved model. Depending on the completion of unseen patches, the intersection can be composed of models reconstructed from any rotational axis. The MSE of intersected models are shown in Table 5.5, and some rendered models are demonstrated in Fig. 5.17 to 5.19. It is noted that the intersection of model is actually an averaging of gray levels from corresponding points in the volumes.

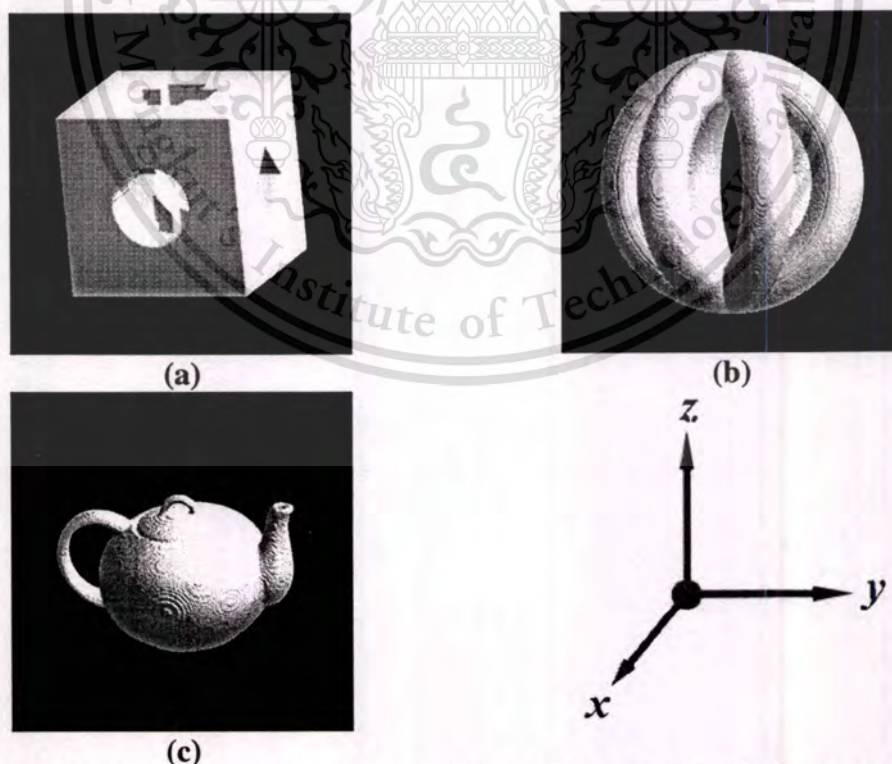


Fig. 5.16 CG Concave models for simulation, (a) the holed cube (Az -15, El -15), (b) the jointed tori (Az -10, El 0), and (c) the Boston teapot (Az -15, El -25)

Table 5.5 MSE of the reconstructed models by different axes of rotation*

Model	Axis of Rotation						
	X	Y	Z	$X \cap Y$	$X \cap Z$	$Y \cap Z$	$X \cap Y \cap Z$
Cube	16.427	10.340	15.744	3.794	3.712	4.314	3.978
Tori	44.705	40.406	18.557	22.609	7.138	9.328	7.194
Teapot	356.695	324.451	338.633	330.517	335.535	327.988	334.188

* 36 projections in the half plane, nearest-neighbor interpolation



Fig. 5.17 The holed cubes reconstructed from the rotation with respect to, (a) X axis, (b) Y axis, and (c) $X \cap Y$

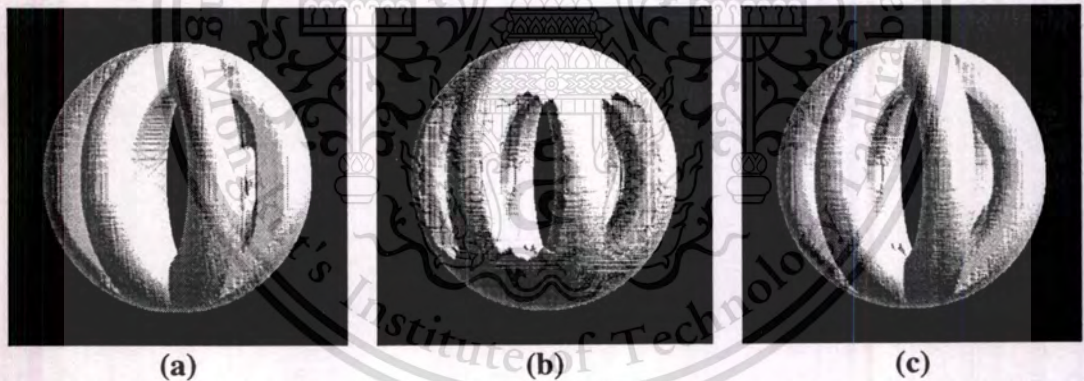


Fig. 5.18 The jointed tori reconstructed from the rotation with respect to, (a) X axis, (b) Z axis, and (c) $X \cap Z$

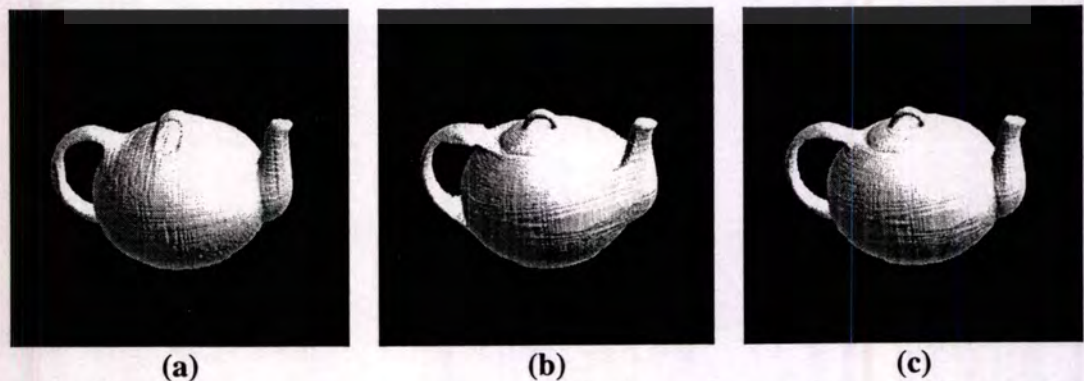


Fig. 5.19 The Boston teapot reconstructed from the rotation with respect to, (a) Y axis, (b) Z axis, and (c) $Y \cap Z$

This material is reserved for educational use only, not allowed for commercial use.

Forbidden to modify the content, and cite the document when use.

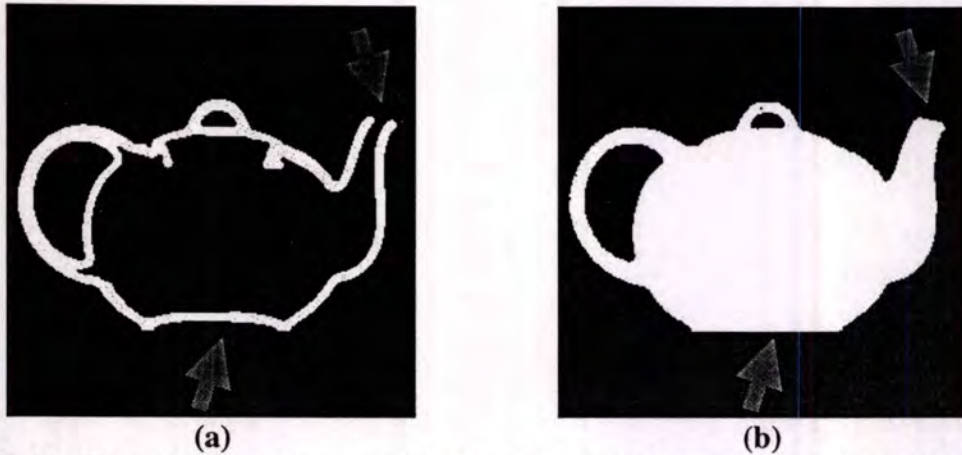


Fig. 5.20 The cutaway views at x of 128 of (a) the original teapot, (b) the $X \cap Y \cap Z$ teapot, showing the flaws to reconstruct a totally-concave object

Conspicuously, the MSE of the double-intersected cubes and tori, $X \cap Y$, $X \cap Z$, and $Y \cap Z$, reduce from their parents as foreseen. However, the triple-intersected volumes, $X \cap Y \cap Z$, do not give any further reduction in error. For the teapot, the intersection scheme seems useless because of the absence of details inside the pot which are totally blinded from every viewpoint (see Fig. 5.20). This is not exactly right since the outer shapes of the intersected models are still improved.

5.3.2 Implementation

The object used to do the implementation is the wood cat shown in Fig. 5.21. This object is rotated and shot for 36 projections in the half respecting to two orthogonal axes marked by the arrows. The reconstructed models are demonstrated in Fig. 5.22 and 5.23. The first model rotated around Z axis has the partially concave problem on its neck and ears whereas the second model rotated around X has the problem on its legs. As a result, the combination of these two models can eliminate the lapse from the occlusion problem.

However, the combination process in the real situation is more complicated than that in the simulation case because two reconstructed models are not aligned harmonically at the beginning and the good alignment is hard to obtain. The easier alignment is done mathematically with the volumetric data by the image registration technique [53]. There are many registration techniques proper for different task. The *landmark-based registration* is the easiest way if some landmarks of the object are known. But the cat has not enough exact landmark. The *iterative closet points (ICP)* technique [54] is selected in this case. It is done by extracting the hundreds of the coordinates from the surfaces of the models, and calculating repeatedly to find the transforming function which gives the least error between two sets of coordinates.

After the registration process is completed, the models are combined to produce the improved model. The improved model is illustrated in Fig. 5.24. Now the neck, the ears, and the legs of the model are improved obviously.

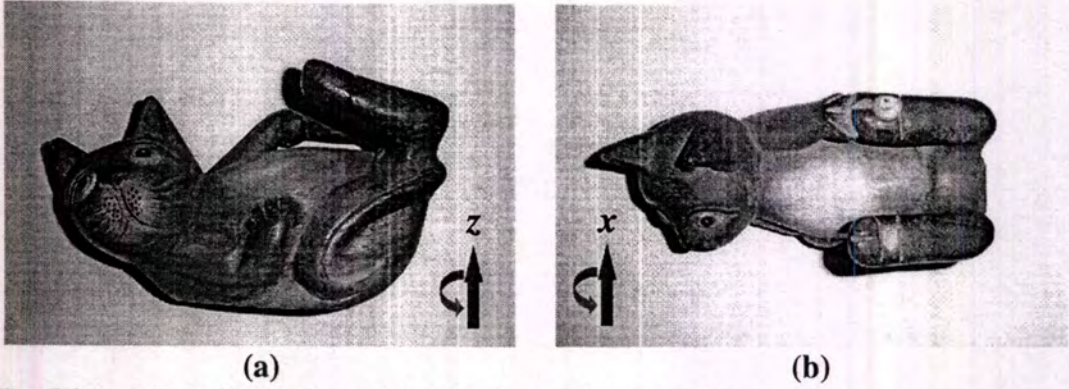


Fig. 5.21 Original wood cat, (a) side view and (b) top view

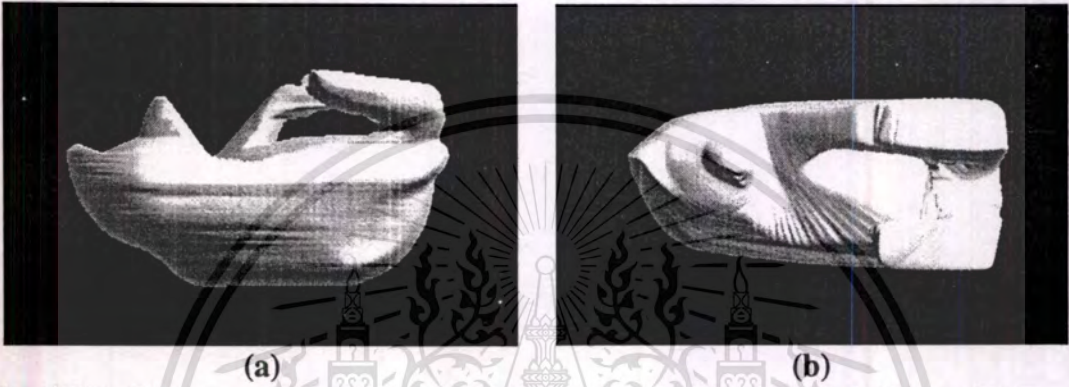


Fig. 5.22 First reconstructed model along Z axis, (a) side view and (b) top view



Fig. 5.23 Second reconstructed model along X axis, (a) side view and (b) top view

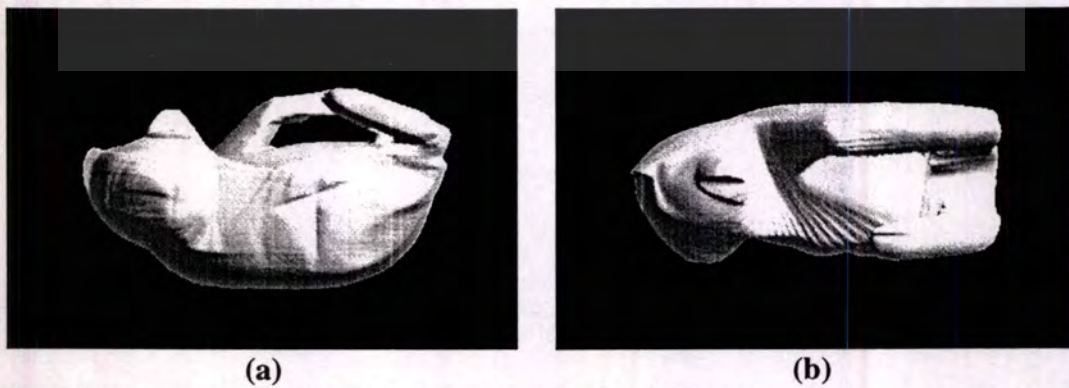


Fig. 5.24 Improved model, (a) side view and (b) top view

Chapter 6

Applications

In the earlier chapters, the process of acquiring the volumetric data of the object by the tomography is presented. Consequently, several applications can derive the benefits from the volume of data. Some of the applications are demonstrated in this section, including 3D shape modeling and geometric measurements.

6.1 3D Modeling

Tending to make the photorealistic scene from raw data, 3D visualization techniques are divided into 2 majority classes with the different characteristics, the surface rendering technique [55] and the volume rendering technique [56]. The surface rendering technique is used to visualize the shape of the object and the spatial relation among these objects by extracting an iso-surface from the data, while the volume rendering allows the entire data to be visualized simultaneously with the classification of features by different values of color and alpha channel at each voxel. Accordingly, the volume rendering technique is much more computationally expensive than the surface rendering.

When only the surface of the object is needed regardless of an internal structure, it is advised to use the surface rendering techniques, the most prominent technique of which is the marching cube [57]. This technique uses the divide-and-conquer strategy to complete the surface; it breaks up the volumetric data into a number of small cubes and matches each cube with the pre-calculated surface pattern. Hence, it delivers the continuous surface made up of an enormous number of linked triangles. However, the marching cube only illustrates the first-order interpolated frontier of the object. The rendering technique together with the Gourad [58] and Phong [59] shading and illumination can closely resemble the real surface properties which response to the specula and ambient lights.

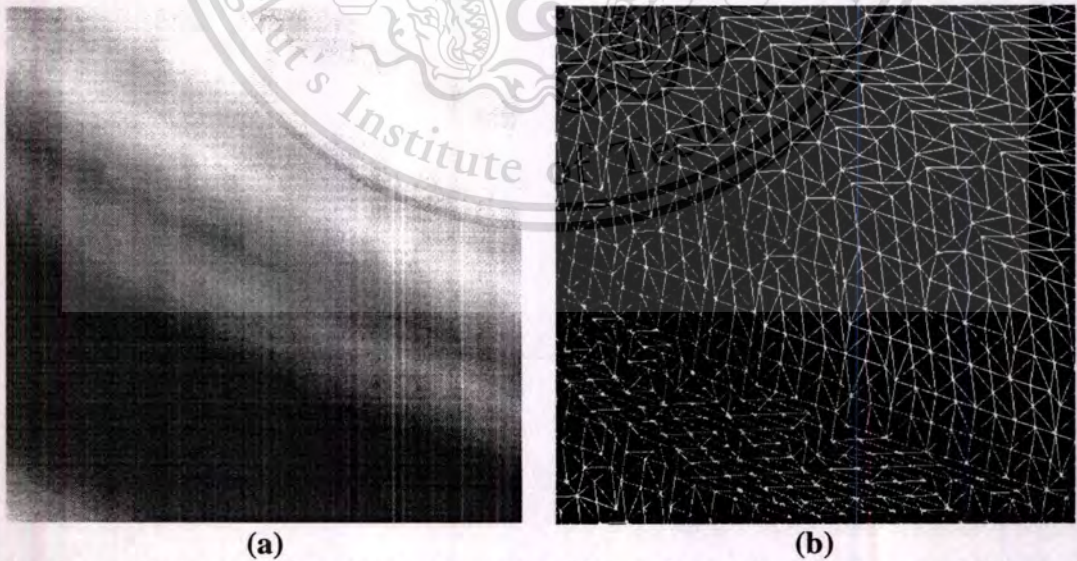


Fig. 6.1 Surface of the object from Marching cubes, (a) closed-up and (b) mesh representation

Table 6.1 The attributes of the reconstructed objects

Object	Width × Height × Depth (voxels)	Number of Projections*	Angle Interval (degrees)	Scale (pixel/cm)	Height (cm)	Triangle Count
Metallic Sphere	256 × 256 × 256	20	9	54.15	8.2	466,872
Woodcarving	256 × 256 × 256	20	9	36.57	7.1	367,488
Foam Cube	256 × 256 × 161	22	8.182	87.27	1.65	274,264
Ceramic Cup	256 × 256 × 200	18	10	N/A	N/A	334,044
Mannequin	256 × 256 × 436	45	4	26.81	16	670,148
Roman Doll	256 × 256 × 375	30	6	43.26	8.6	551,608
Hourglass	256 × 256 × 512	22	8.182	48.19	10.5	1,291,608
Foam Head	256 × 256 × 305	30	6	10.07	30	584,460
Miniature Truck	256 × 512 × 256	45	4	36.77	6.2	1,255,618
Chinese Doll (Sec. 6.1.2)	256 × 256 × 480	44**	8.182	N/A	N/A	264,136
Cat (Sec. 5.3.2)	160 × 320 × 160	36	5	N/A	N/A	906,392

* Half-plane projection

** Full-plane projection

The surface of the object is created by segmenting the reconstructed data, calculating normal vectors for every polygon from gray levels of the same information, and then rendering using technique described above.

Regarding to the conditions verified in the preceding chapter, the volumetric data of assorted objects, whose surfaces are either Lambertian or non-Lambertian type, are reconstructed from their corresponding sequences of photographs, and all of the attributes are recorded in Table 6.1. Subsequently, all of the investigated objects are shown in Fig. 6.2 to Fig. 6.12 along with their solid models rendered in the distinctive viewpoints (cube size of the marching cube equals to one). It is noted that some objects use the number of projections twice as many as the specific value to make the gradient smoother.

Form the results, the process achieves successfully on the simple-shaped objects such as the metallic sphere, the woodcarving, the foam cube, the mannequin, and the foam head. Nevertheless, some information is missing in the high-detailed object caused by the totally concave problem. The ceramic cup and the roman doll are the best examples of this problem; the empty space inside the cup is completely filled with over-thresholded voxels (Fig. 6.5) while the shield of roman doll is merged with his arm (Fig. 6.9). For the miniature truck, the perspective occlusion seems to be the major problem that disfigures the model. Besides, another problem is that the surfaces of the rendered objects are a bit coarse even though those of the sources are not; this problem results from the first-ordered interpolation of the rendering algorithm together with the aliasing artifacts. In spite of some shortcoming, it can be inferred that shapes of the objects are almost analogous to their originals regardless of the surface properties.

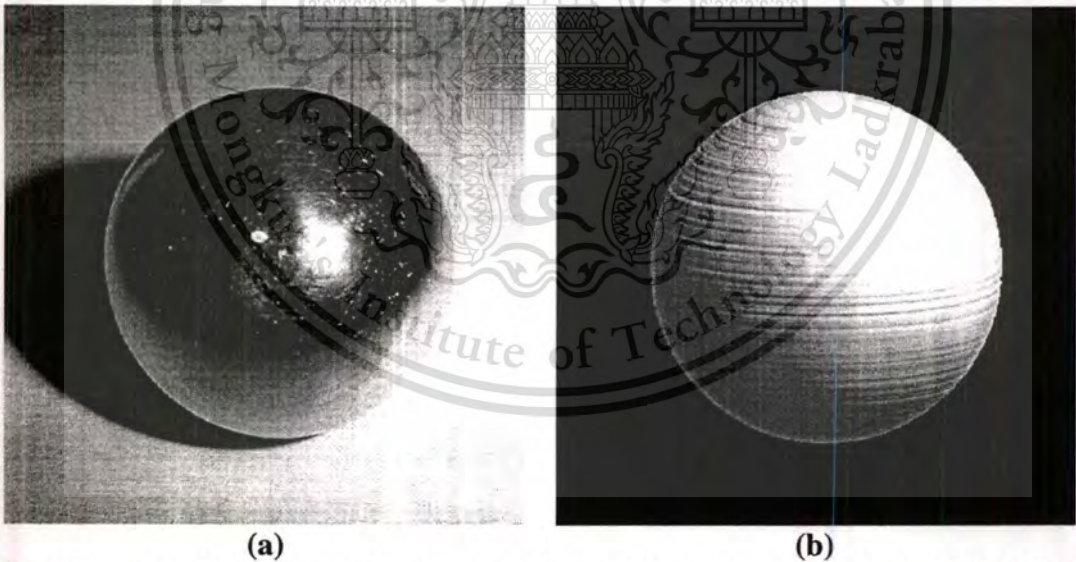
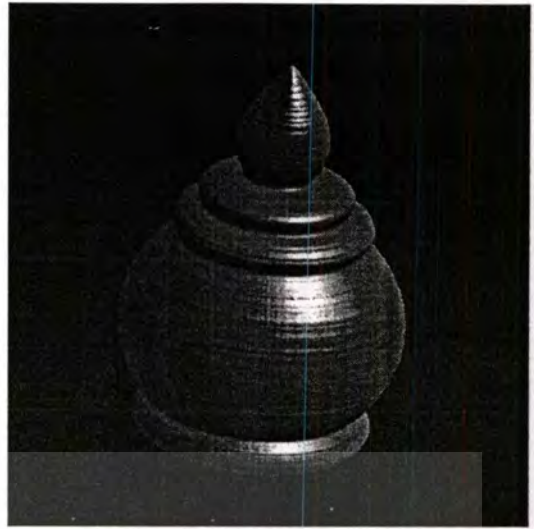


Fig. 6.2 Metallic sphere, (a) actual model and (b) rendered model (Az.0,El.10,Tw.0)



(a)



(b)

Fig. 6.3 Woodcarving, (a) actual model and (b) rendered model (Az.15,El.25,Tw.0)



(a)



(b)

Fig. 6.4 Foam cube, (a) actual model and (b) rendered model (Az.-40,El.30,Tw.-20)



(a)



(b)

Fig. 6.5 Ceramic cup, (a) actual model and (b) rendered model (Az.70,El.15,Tw.10)

This material is reserved for educational use only, not allowed for commercial use.

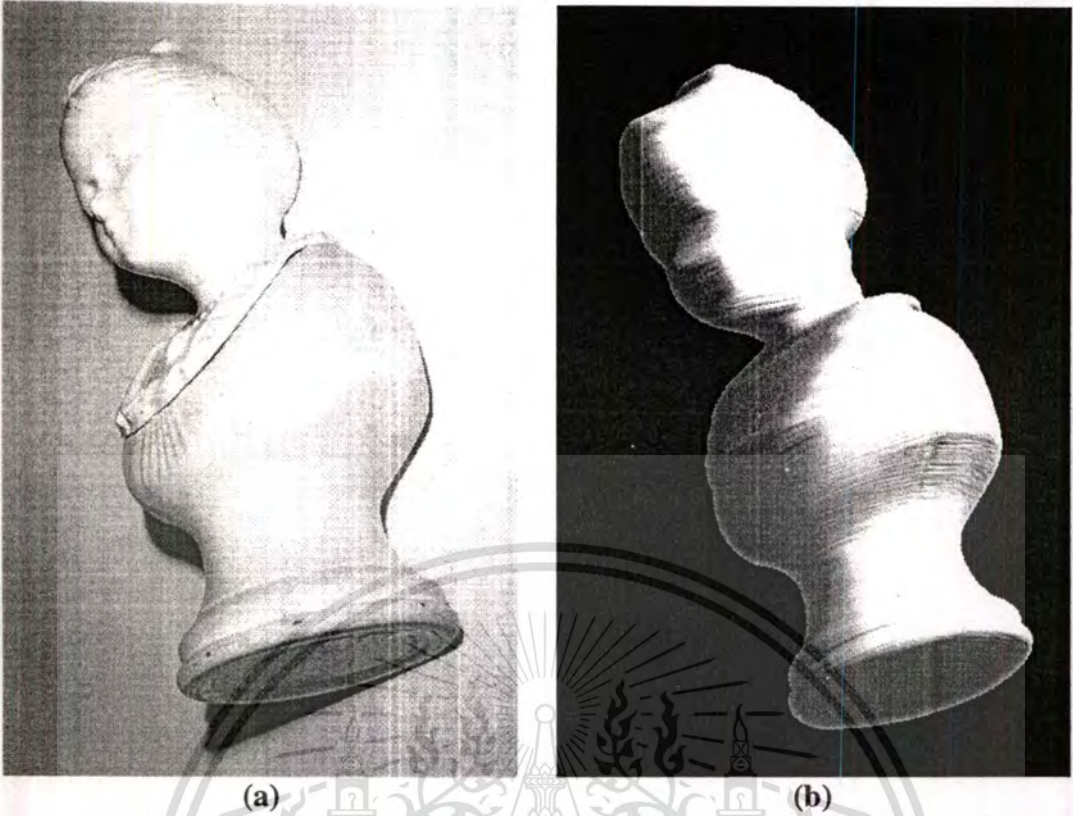


Fig. 6.6 Mannequin, (a) actual model and (b) rendered model (Az.-45,El.-25,Tw.35)

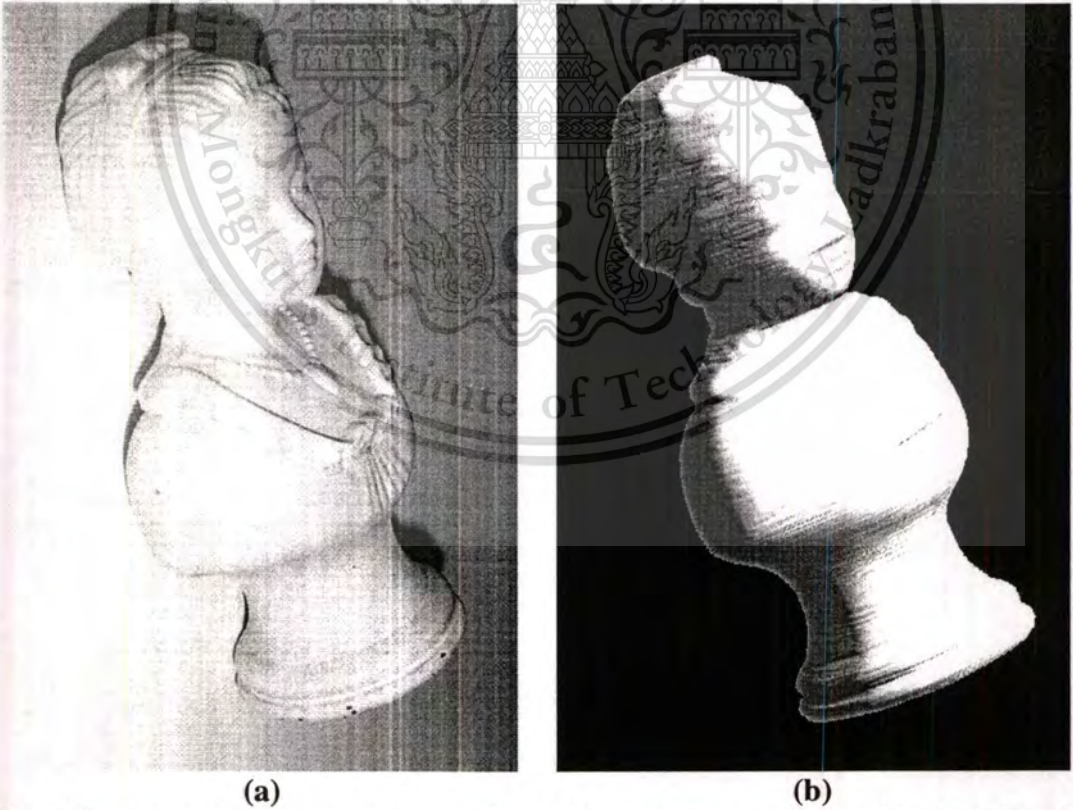


Fig. 6.7 Mannequin, (a) actual model and (b) rendered model (Az.50,El.15,Tw.35)

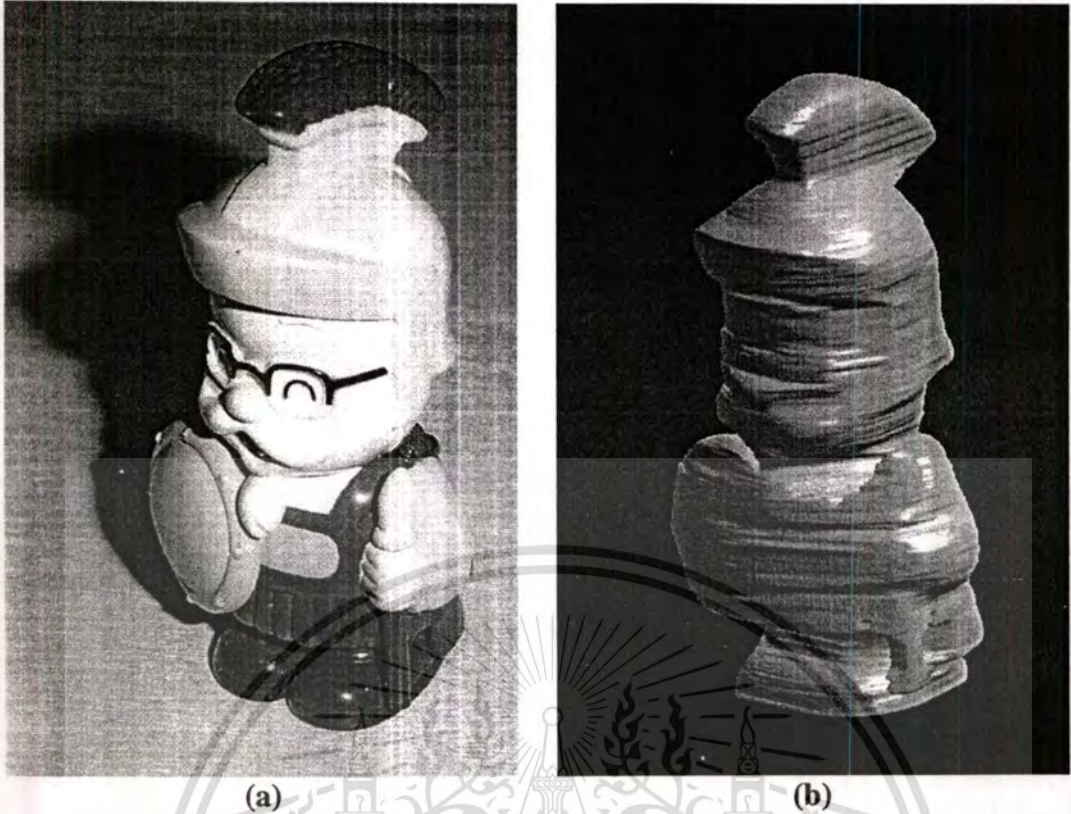


Fig. 6.8 Roman doll, (a) actual model and (b) rendered model (Az.-40,El.20,Tw-10)

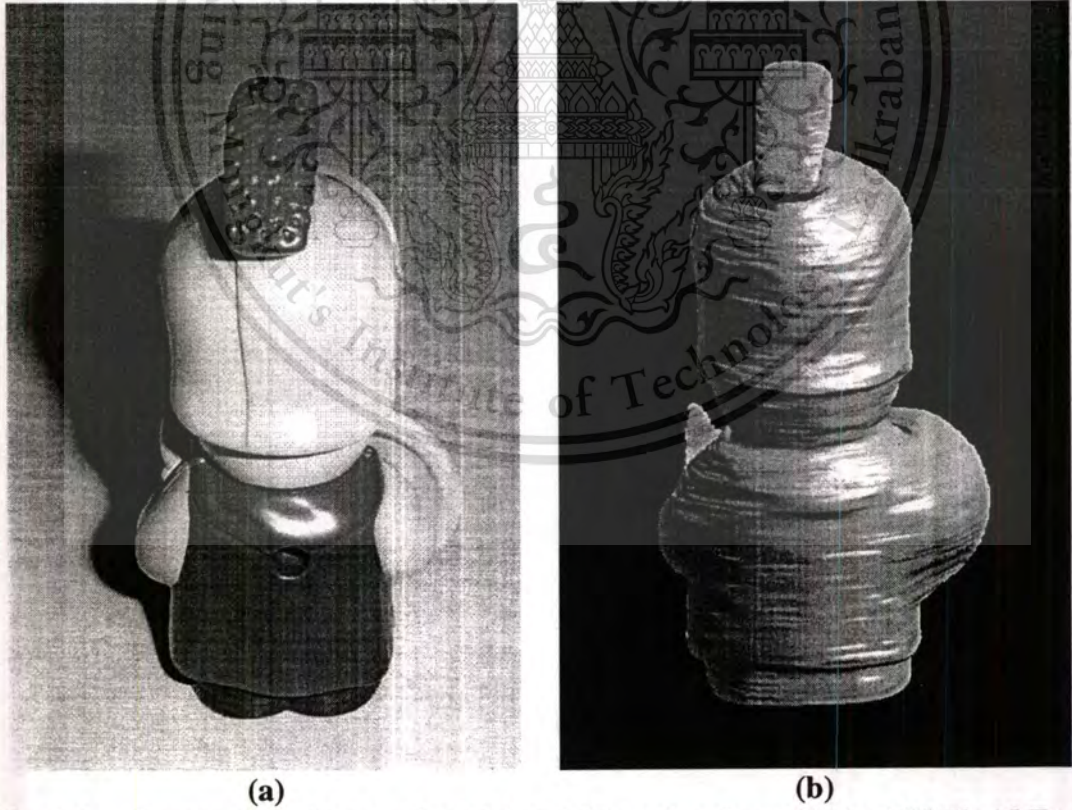


Fig. 6.9 Roman doll, (a) actual model and (b) rendered model (Az.175,El.-15,Tw.0)

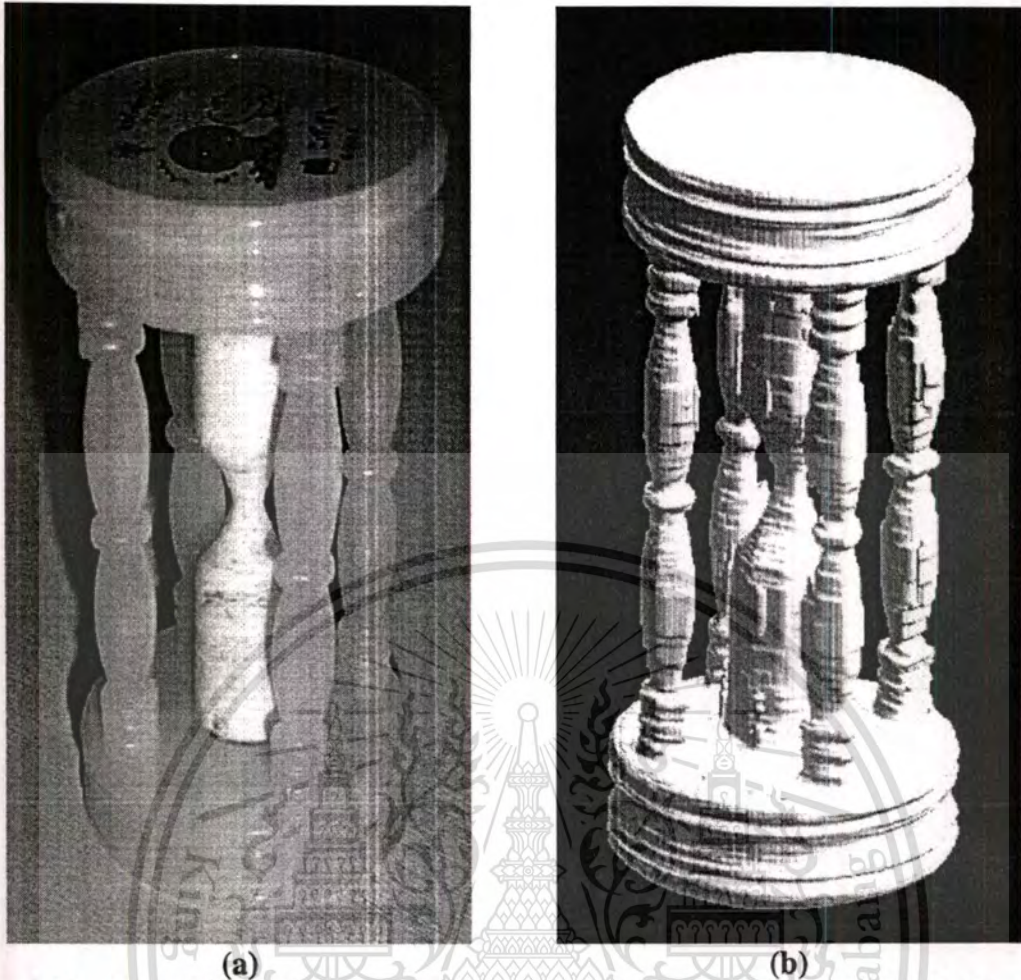


Fig. 6.10 Hourglass, (a) actual model and (b) rendered model (Az.-20,El.25,Tw.-10)

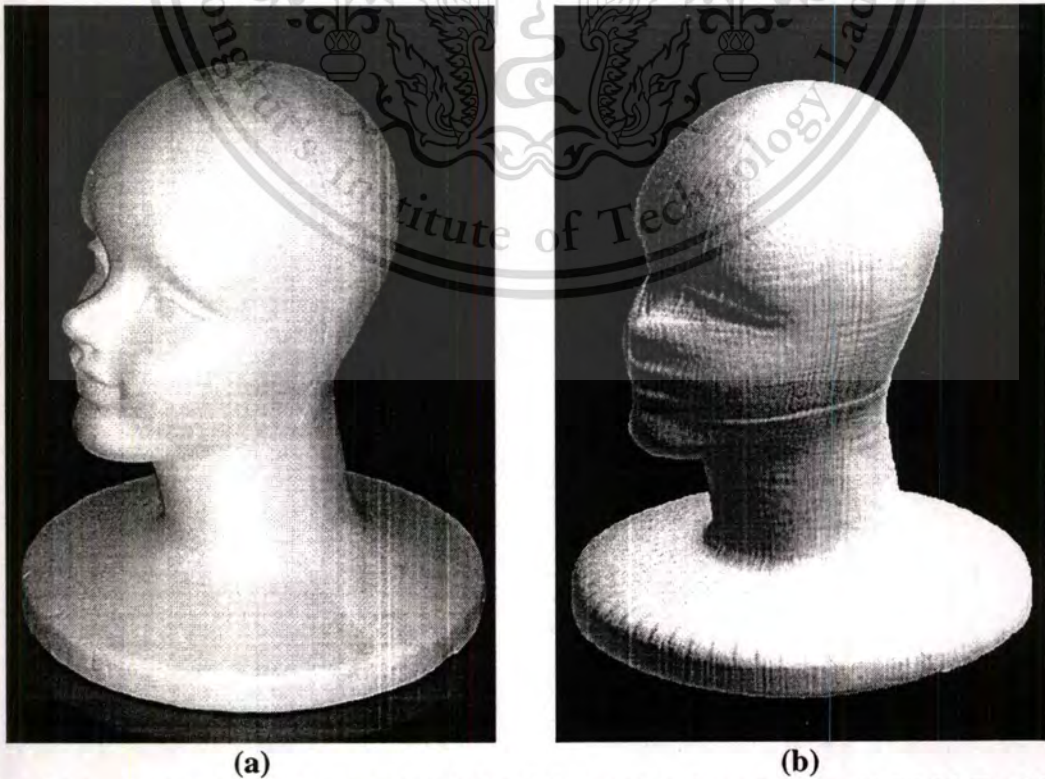


Fig. 6.11 Foam head, (a) actual model and (b) rendered model (Az.40,El.30,Tw.20)

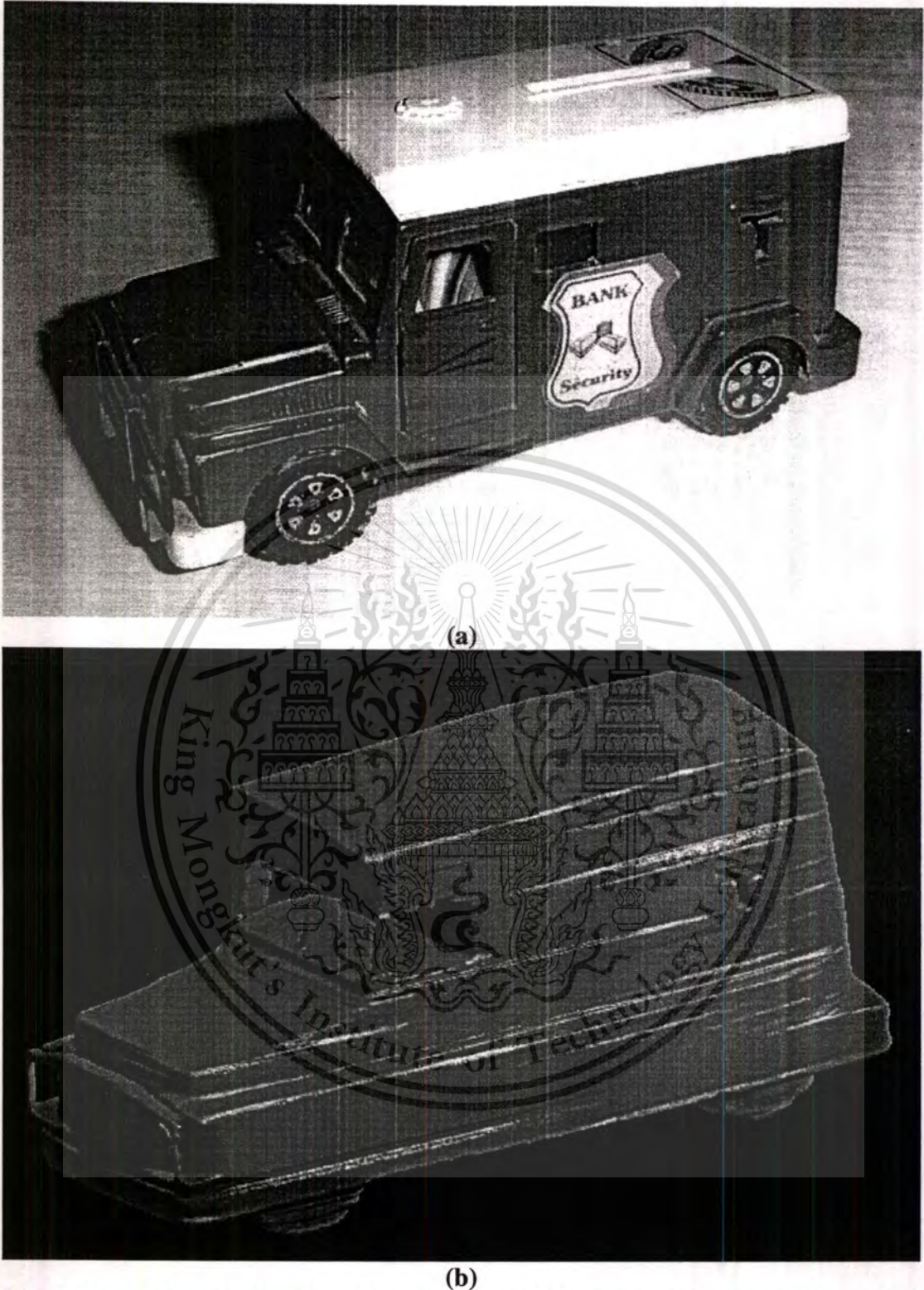


Fig. 6.12 Miniature truck, (a) actual model and (b) rendered model
(Az.120,El.-40,Tw.-30)

6.2 Geometric Measurements

In this part, the volumes and surface areas of various objects are explicitly measured from their stacks of cross sections and compared to their real values. In order to obtain the physical instead of pixel unit, the scale of voxel or pixel per physical dimension must be known exactly.

6.2.1 Volume Measurement

One of the concerned researches [38] has committed the volume measurement of the stack of data by using the indirect technique. From Fig. 6.13 by extracting the set of the coordinates located on the edge of each slice, the area of the slice can be summed up from the magnitudes of cross products of vectors stretched from the origin to edge's coordinates, or

$$Area = \frac{1}{2} \sum_{n=0}^N |\vec{U}_n \times \vec{U}_{n+1}| \quad (6.1)$$

where N is the number of edge's coordinates, and \vec{U} is the vector. As a result, the volume of data is obtainable by multiplying the area with the thickness of each slice and then adding up throughout the stack. Nevertheless, the result of this technique would not be acceptable if the object had the concave hull, which was the common feature of most objects (see Fig. 6.13). Hence, to subdue this problem, the straightforward technique by counting the number of over-thresholded voxels is preferable, followed by converting it to the physical value using Eq. 6.2.

$$Volume = \frac{N}{(ppl.)^3} \quad (6.2)$$

where N is the number of over-thresholded voxels, and ppl is the pixel per a physical length (e.g. centimeter). The results of volume measurement are shown in Table 6.2 along with the scales, true volumes measured by the Eureka, and the errors in percent.

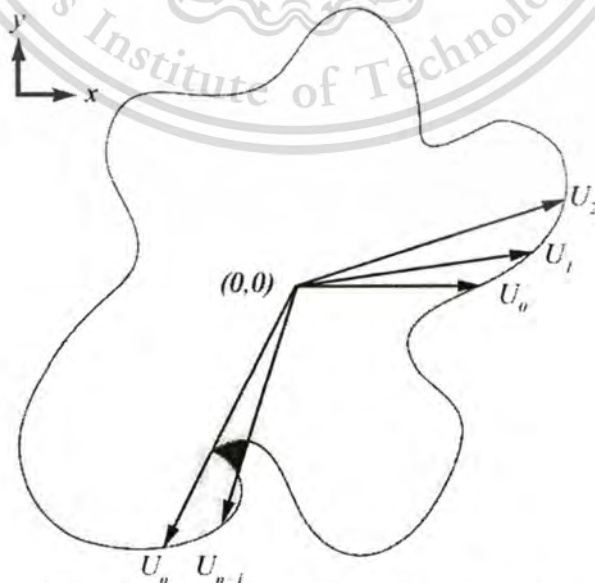


Fig. 6.13 Measuring the area (volume) of the object by using cross products with each slice. The error occurring at the highlighted portion

This material is reserved for educational use only, not allowed for commercial use.

Forbidden to modify the content, and cite the document when use.

Table 6.2 The estimated volume compared to the true volume of the specified objects

Object	Scale (pixel/cm) ³	True Volume (cm) ³	Estimated Volume (cm) ³	Error (%)
Metallic Sphere	158779.85	36.087	35.344	-2.059
Woodcarving	48907.43	70.00	65.408	-6.560
Foam Cube	664652.94	4.492	5.05	12.422
Mannequin	19270.39	310.00	310.525	0.169
Roman Doll	80957.96	53.00	54.428	2.694
Hourglass	111910.49	67.50	70.394	4.287
Foam Head	1021.15	N/A	4770.261	N/A
Miniature Truck	49714.25	N/A	301.928	N/A

The differences between the exact and estimated volumes are remarkably low for such convex-shaped objects as the mannequin or the metallic sphere. Contrarily, the calculated volume of the sharp-cornered object like the foam cube is significantly high. This mistake arises from the improper positioning of the object and the inadequate viewpoint.

6.2.2 Surface Measurement

As another application, the surface area of the object can be approximately measured with the assistance of the marching cube algorithm [57]. By interpolating the smooth surface of the object with a set of primitive triangles connected incessantly, the area of every triangle can be readily calculated and summed up to represent the total surface area. In the Table 6.3 are shown the areas of triangles calculated by the cross-product method for the 15 primary cube cases. The dimensions of cube are set to single pixel.

Table 6.3 The area of triangles contained in each cube created by the marching cube algorithm.
















Cube Case	Triangulated Cube	Area (pixel) ²	Cube Case	Triangulated Cube	Area (pixel) ²
0		0.0000	8		1.0000
1		0.2165	9		1.2990
2		0.7071	10		1.4142
3		0.4330	11		1.5731
4		0.4330	12		1.3660
5		1.1495	13		0.8660
6		0.9236	14		1.5731
7		0.6495			

Table 6.4 The estimated surface area compared to the true area of the specified object

Object	Scale (pixel/cm) ²	True Area (cm) ²	Estimated Area (cm) ²	Error (%)
Metallic Sphere	2932.22	52.810	58.949	11.625
Woodcarving	1337.36	N/A	102.472	N/A
Foam Cube	7616.05	16.335	17.656	8.087
Mannequin	718.78	N/A	355.679	N/A
Roman Doll	1871.43	N/A	114.054	N/A
Hourglass	2322.28	N/A	224.192	N/A
Foam Head	101.405	N/A	2290.828	N/A
Miniature Truck	1352.03	N/A	392.370	N/A

The results shown in Table 6.4 are devoid of real values, which are generally difficult to carry out. Even so, the conclusion can be made from the limited evidences that the estimated surface areas are larger than they should be, around 10 percent, resulting from the existence of rough surface. Decreasing the area by the compensation can improve the result.

Chapter 7

Conclusions and Suggestions

Eventually, all the goals have been accomplished successfully, and they will be paraphrased shortly in this chapter. Additionally, there are a few suggestions that should be declared in order to make the result more improved and more useful.

7.1 Conclusions

The 3D shape extraction using photographic tomography is studied extensively. The main idea of the method is that the tomographic imaging is used to reconstruct the stack of pseudo cross-sectional images from a series of photographs taken around the object. The shape of the stack can closely resemble the shape of original object.

Compared with other 3D shape extraction techniques, the equipment used to collect the data for this technique is much lesser in complexity. It mainly consists of the rotating platform and the digital camera which is locally available and affordable.

The optimum condition of each parameter to reconstruct the shape of the object has been verified carefully. The first parameter is the reconstruction technique; the modified backprojection gives the best result within the shortest time. The second is the number of projections, which should be more than 20 for the half plane. The last is the reconstruction geometry; the parallel-backprojection algorithm could be applied if the distance between the model and camera were greater than 16 times of the model's thickness.

The only lapse that makes the photographic tomography imperfect is the concave occlusion, the total concave and the partial concave. The solution to the partially concave occlusion is to rotate and reconstruct the object respecting to more than one axis, and then combine the registered outputs together. Conversely, the solution to the totally concave occlusion is still obscure.

Several applications, including the 3D modeling and the geometric measurements, have been demonstrated. For the modeling, the marching cube algorithm along with the shading and illumination model is applied to the volumetric data to provide the 3D visualization with both bogus and true colors. The results have a similar appearance to the originals except for the occluded area. For the geometric measurements, the volume measurement can closely estimate the volume of the object whereas the surface measurement can estimate the area not as good as it could.

Despite some drawbacks, the proposed technique is tested successfully to generate the shape of a variety of objects.

7.2 Suggestions

Because of the storage size of the reconstructed volume, the awareness of reduction of the volume is important. Excluding the data compression scheme, the curve fitting technique [60, 61] is interesting. Because only the surface is the main feature of the entire volume, it is a good idea to discard other unnecessary data. The artificial surface can fit the real surface of the volume by means of a few control points, and all that have to be stored are the controls points' coordinates. This scheme not only tremendously lessens the data size, but it also removes the noises that make the reconstructed surface rough.

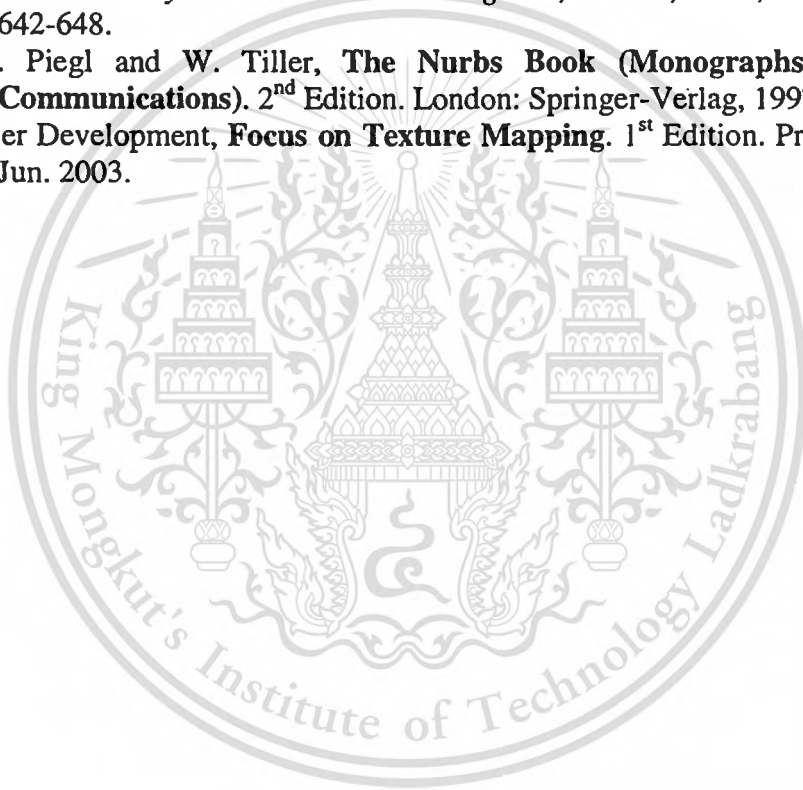
References

- [1] J. Radon, "Über die Bestimmung von Funktionen durch ihre Integralwerte langs gewisser Mannigfaltigkeiten," *Berichte Sachsische Akademie der Wissenschaften*, Leipzig, Math. — Phys. Kl. vol. 69, 1917. pp. 262-267.
- [2] A. A. Kirillov, "On a Problem of I.M.," *Gelfand. Sov. Math. Dokl.*, vol. 2, 1961. pp. 268-269.
- [3] R. N. Bracewell, "Strip Integration in Radio Astronomy," *Aust. J. Physics*, vol. 9, 1956. pp. 198-217.
- [4] A. C. Kak and M. Slaney, **Principles of Computerized Tomographic Imaging**. New York: IEEE Press, 1988.
- [5] H. M. Iyer and K. Hirahara, Ed., **Seismic Tomography: Theory and Practice**. Chapman & Hall. 1993.
- [6] J. L. Ackerman and W. A. Ellingson, Ed., **Advanced Tomographic Imaging Methods for the Analysis of Materials**. Material Research Society, Sep. 1991.
- [7] R. A. Williams and M. S. Beck, Ed., **Process Tomography: Principles, Techniques and Applications**. Oxford: Butterworth-Heinemann, Ltd., 1995.
- [8] The National Library of Medicine, "The Visible Human Project," [Online]. Available: www.nlm.nih.gov/research/visible/visible_human.html. 2003.
- [9] TeraRecon Inc., "Geoscience Image Gallery," [Online]. Available: http://www.terarecon.com/gallery/geo_gallery.html. 2003.
- [10] Process Tomography Limited, "Applications," [Online]. Available: <http://www.tomography.com/apps.htm>. 2003.
- [11] TeraRecon Inc., "TeraRecon - 3D Cone Beam CT," [Online]. Available: http://www.rtviz.com/products/3dct_usage_prod.html. 2003.
- [12] S. T. Barnard and M. A. Fischler, "Computational Stereo," *ACM Computing Surveys*, vol. 14, no. 4, 1982. pp. 553-572.
- [13] U. R. Dhond and J. Aggarwal, "Structure from Stereo - A Review," *IEEE Trans. Systems, Man, and Cybernetics*, vol. 19, no. 6, 1989. pp. 1489-1510.
- [14] T. Bosch, N. Servagent, R. Chellali, and M. Lescure, "Three-Dimensional Object Construction Using a Self-mixing Type Scanning Laser Range Finder," *IEEE Trans. Instrumentation and Measurement*, vol. 47, no. 5, 1998. pp. 1326-1329.
- [15] Center for Machine Perception (CMP), "Laser Plane Range Finder," [Online]. Available: <http://cmp.felk.cvut.cz/>.
- [16] D. M. Meadows, W. O. Johnson, and J. B. Allen, "Generation of Surface Contours by Moiré Pattern," *Applied Optics*, vol. 9, 1970. pp. 942-947.
- [17] B. K. P. Horn. "Shape from Shading: A Method for Obtaining the Shape of a Smooth Opaque Object from One View." Ph.D. Thesis of Massachusetts Inst. of Technology, 1970.
- [18] R. Zhang, P.-S. Tsai, J. E. Cryer, and M. Shah, "Shape from Shading: A Survey," *IEEE Trans. Pattern Analysis and Machine Intelligence*, vol. 21, no. 8, Aug. 1999. pp. 690-706.
- [19] B. K. P. Horn, R. S. Szeliski, and A. L. Yuille, "Impossible Shaded Images," *IEEE Trans. Pattern Analysis and Machine Intelligence*. vol. 15, no. 2, Feb. 1993. pp. 166-170.

- [20] W. N. Martin and J. K. Aggarwal, "Volumetric Description of Objects from Multiple Views," *IEEE Trans. Pattern Analysis and Machine Intelligence*, vol. 5, no. 2, 1983. pp. 150-158.
- [21] N. Ahuja and J. Veenstra, "Generating Octrees from Object Silhouettes in Orthographic Views," *IEEE Trans. Pattern Analysis and Machine Intelligence*, vol. 11, no. 2, 1989. pp. 137-149.
- [22] H. Noborio, S. Fukada, and S. Arimoto, "Construction of the Octree Approximating Three-Dimensional Objects by Using Multiple Views," *IEEE Trans. Pattern Analysis and Machine Intelligence*, vol. 10, no. 6, 1988. pp. 769-782.
- [23] M. Potmesil, "Generating Octree Models of 3D Objects from Their Silhouettes in a Sequence of Image," *Computer Vision, Graphics and Image Processing*, vol. 40, 1987. pp. 1-20.
- [24] S. K. Srivastava and N. Ahuja, "Octree Generation from Object Silhouettes in Perspective Views," *Computer Vision, Graphics and Image Processing*, vol. 49, 1990. pp. 68-84.
- [25] R. Szeliski, "Rapid Octree Construction from Image Sequences," *Computer Vision, Graphics and Image Processing: Image Understanding*, vol. 58, no. 1, 1993. pp. 23-32.
- [26] G. Cross and A. Zisserman, "Surface Reconstruction from Multiple Views Using Apparent Contours and Surface Texture," **Confluence of Computer Vision and Computer Graphics**, A. Leonardis, F. Solina, and R. Bajcsy, Ed. Boston: Kluwer, 2000. pp. 25-47.
- [27] P. Eisert, E. Steinbach, and B. Girod, "Multi-Hypothesis, Volumetric Reconstruction of 3-D Objects from Multiple Calibrated Camera Views," *Proc. Int. Conf. Acoustics, Speech, and Signal Processing*, 1999. pp. 3509-3512.
- [28] S. M. Seitz and C. R. Dyer, "Photorealistic Scene Reconstruction by Voxel Coloring," *Int. J. of Computer Vision*, vol. 35, no. 2, 1999. pp. 151-173.
- [29] F. Schmitt and Y. Yemez, "3D Color Object Reconstruction from 2D Image Sequence," *Proc. Int. Conf. on Image Processing*, vol. 3, 1999. pp. 65-69.
- [30] C. R. Dyer, "Volumetric Scene Reconstruction from Multiple Views," **Foundation of Image Understanding**, L. S. Davis, Ed. Boston: Kluwer, 2001. pp. 469-489.
- [31] S. Moezzi, L-C Tai, and P. Gerard, "Virtual View Generation for 3D Digital Video," *IEEE Multimedia*, vol. 4, no. 1, 1997. pp. 18-26.
- [32] G. K. M. Cheung, T. Kanade, J-Y. Bouguet, and M. Holler, "A Real Time System for Robust 3D Voxel Reconstruction of Human Motions," *Proc. Conf. on Computer Vision and Pattern Recognition*, vol. 2, 2000. pp. 714-720.
- [33] S. Moezzi, A. Katkere, D. Kuramura, and R. Jain, "Reality Modeling and Visualization from Multiple Video Sequences," *IEEE Computer Graphics and Applications*, vol. 16, no. 6, 1996. pp. 58-63.
- [34] D. T. Gering and W. M. Wells, III, "Object Modeling Using Tomography and Photography," *Proc. IEEE Workshop on Multi-View Modeling and Analysis of Visual Scenes*, 1999. pp. 11-18.
- [35] A. J. Johnson, D. L. Marks, R. A. Stack, D. J. Brady, and D. C. Munson, "Three-Dimensional Surface Reconstruction of Optical Lambertian Objects Using Cone-Beam Tomography," *Proc. IEEE Conf. on Image Processing*, vol. 2, 1999. pp. 663-667.

- [36] D. L. Marks, R. Stack, A. J. Johnson, D. J. Brady, and D. C. Munson, "Cone-Beam Tomography with a Digital Camera," *Applied Optics*, vol. 40, no.11, Apr. 2001. pp 1795-1805.
- [37] W. Withayachumnankul, C. Pintavirooj, M. Sangworasil, and K. Hamamoto, "3D Shape Recovery Based on Tomography," *Proc. Int. Conf. on Signal Processing*, Beijing, China, Oct. 2002. pp. 784-787.
- [38] C. Pintavirooj and M. Sangworasil, "3D Modeling Based on Radon Transform with Application in Volume Measurement," *Proc. WSCG*, Czech, Feb. 2002. pp. POS33.
- [39] D. L. Marks, R. A. Stack, D. J. Brady, D. Munson, and R. B. Brady, "Visible Cone-Beam Tomography with a Lensless Interferometric Camera," *Science*, vol. 284, 1999. pp. 2164-2166.
- [40] D. L. Marks and D. J. Brady, "Three-Dimensional Source Reconstruction with a Scanned Pinhole Camera," *Optics Letters*, vol. 23, 1998. pp. 820-822.
- [41] D. L. Marks, R. A. Stack, D. J. Brady, and J. van der Gracht, "Three-Dimensional Tomography Using a Cubic-Phase Plate Extended Depth-of-Field System," *Optics Letters*, vol. 24, 1999. pp. 253-255.
- [42] A. C. Kak, "Computerized Tomography with X-Ray Emission and Ultrasound Sources," *Proc. IEEE*, vol. 67, 1979. pp. 1245-1272.
- [43] H. H. Stark, J. W. Woods, I. Paul, and R. Hingorani, "Direct Fourier Reconstruction in Computer Tomography," *IEEE Trans. Acoustics, Speech and Signal Processing*, vol. 29, 1981. pp. 237-245.
- [44] A. C. Kak, "Tomographic Imaging with Diffracting and Non-Diffracting Source," *Array Signal Processing*, S. Haykin, Ed. Englewood Cliffs, NJ: Prentice-Hall, 1985.
- [45] L. A. Feldkamp, L. Davis, and K. Kress, "Practical Cone-Beam Algorithm," *Journal of the Optical Society of America*, vol. 1, Jun. 1984. pp. 612-619.
- [46] R. Gordon, R. Bender, and G. T. Herman, "Algebraic Reconstruction Techniques (ART) for Three Dimensional Electron Microscopy and X-ray Photography," *Journal of Theoretical Biology*, vol. 29, pp. 471-481, 1970.
- [47] P. Gilbert, "Iterative Method for the Reconstruction of Three Dimensional Objects from Their Projection," *Journal of Theoretical Biology*, vol. 36, 1972. pp. 105-117.
- [48] A. H. Andersen and A. C. Kak, "Simultaneous Algebraic Reconstruction Technique (SART): A Superior Implementation of the ART Algorithm," *Ultrasonic Imaging*, vol. 6, Jan. 1984. pp. 81-94.
- [49] H. A. Anders, "Algebraic Reconstruction in CT from Limited Views," *IEEE Trans. Medical Imaging*, vol. 8, no. 1, 1989. pp. 50-55.
- [50] M. Born and E. Wolf, **Principles of Optics: Electromagnetic Theory of Propagation, Interference and Diffraction of Light**. 6th Edition. Oxford: Pergamon Press, 1989.
- [51] J. A. Green, **Medical Image Processing: The Mathematics of Medical Imaging**. 2nd Edition. Greenwood Research, 2002.
- [52] Volvis, "Boston Teapot," [Online]. Available: <http://www.volvis.org/>. 2003.
- [53] J. V. Hajnal, D. J. Hawkes, and Derek Hill, Ed., **Medical Image Registration**. CRC Press, 2001.
- [54] P. J. Besl and N. D. McKay, "A Method for Registration of 3-D Shapes," *IEEE Trans. Pattern Analysis and Machine Intelligence*, vol. 14, no. 2, Feb. 1992. pp. 239-256.

- [55] M. R. Stytz, G. Frieder, and O. Frieder, "Three-Dimensional Medical Imaging: Algorithms and Computer Systems," *ACM Computing Surveys*, vol. 23, no. 4, Dec. 1991. pp. 421-499.
- [56] B. Lichtenbelt, R. Crane, and S. Naqvi, **Introduction to Volume Rendering (Hewlett-Packard Professional Books)**. Prentice Hall PTR., 1998.
- [57] W. E. Lorensen and H. E. Cline, "Marching Cubes: A High Resolution 3D Surface Construction Algorithm," *Computer Graphics (Proc. SIGGRAPH)*, vol. 21, no. 3, Jul. 1987. pp. 163-169.
- [58] H. Gouraud, "Continuous Shading of the Curved Surface," *IEEE Trans. Computers*, vol. 20, no. 6, 1971. pp. 623-629.
- [59] B. T. Phong, "Illumination for Computer Generated Pictures," *Communications of the ACM*, vol. 18, no. 6, 1975. pp. 311-317.
- [60] F. S. Cohen, W. Ibrahim, and C. Pintavirooj, "Ordering and Parameterizing Scattered 3D Data for B-Spline Surface Approximation," *IEEE Trans. Pattern Analysis and Machine Intelligence*, vol. 22, no. 6, Jun. 2000. pp. 642-648.
- [61] L. A. Piegl and W. Tiller, **The Nurbs Book (Monographs in Visual Communications)**. 2nd Edition. London: Springer-Verlag, 1997.
- [62] Premier Development, **Focus on Texture Mapping**. 1st Edition. Premier Press, Jun. 2003.



Appendix

3D Modeling with True-Colored Mapping

In Section 6.1, only the shapes of the models are rendered regardless of their factual colors. In order to display them with the true colors, the supplementary process must be brought up. Generally, the texture mapping technique [60] is employed to attain this option; however, this technique requires user's cooperation to identify matching points between the texturing image and the rendered model, and the specula artifacts of the non-Lambertian surface make the texture look weird while the viewpoint is changed. Another technique, which takes an advantage from the tomography, needs less collaboration from the user due to the consistency of the geometry. The diagram of latter technique illustrated in Fig. A.1 explains how to obtain the colored cross-section in an RGB mode.

From the diagram, the set of color photographs serving as the projections are split into 4 components composed of red, green, blue, and alpha channel. The alpha channel is actually the silhouetted projection used in the preceding subject. These 4 channels of projections are *separately and simultaneously* backprojected and normalized to impede the saturation of individual color. Consequently, the outputs of the reconstruction are 4 stacks of cross sections ready to be rendered by the modified marching-cube algorithm. In the modified algorithm, all of the color channels are combined and converted into the true-color cross-sections and then segmented to separate the foreground from the background using solid cross-sections reconstructed from the alpha channel.

The original model, the colorless model, and the true-colored model of the Chinese doll in the similar viewpoints are revealed in Fig. A.2 to Fig. A.4. Even though the projections have the specula artifacts because of the shiny surface of the object, the model rendered using color plates from the tomography does not express such persistent artifacts (the occurrences of specula in the rendered model are generated later from the lighting model) because the spots of luster are averaged down during the backprojection process. The separations between colors in the vertical direction of the model is apparent, e.g. in the junction of shirt and trousers, whereas those in the horizontal direction are a bit obscure, e.g. in the joints of body and arms. The model's color resulting from smearing of the backprojection is faded out compared with that of the archetype. However, the overall outcome is acceptable if the process is considered as automation. It is noted that the rough surface is caused by the limit of image resolution.

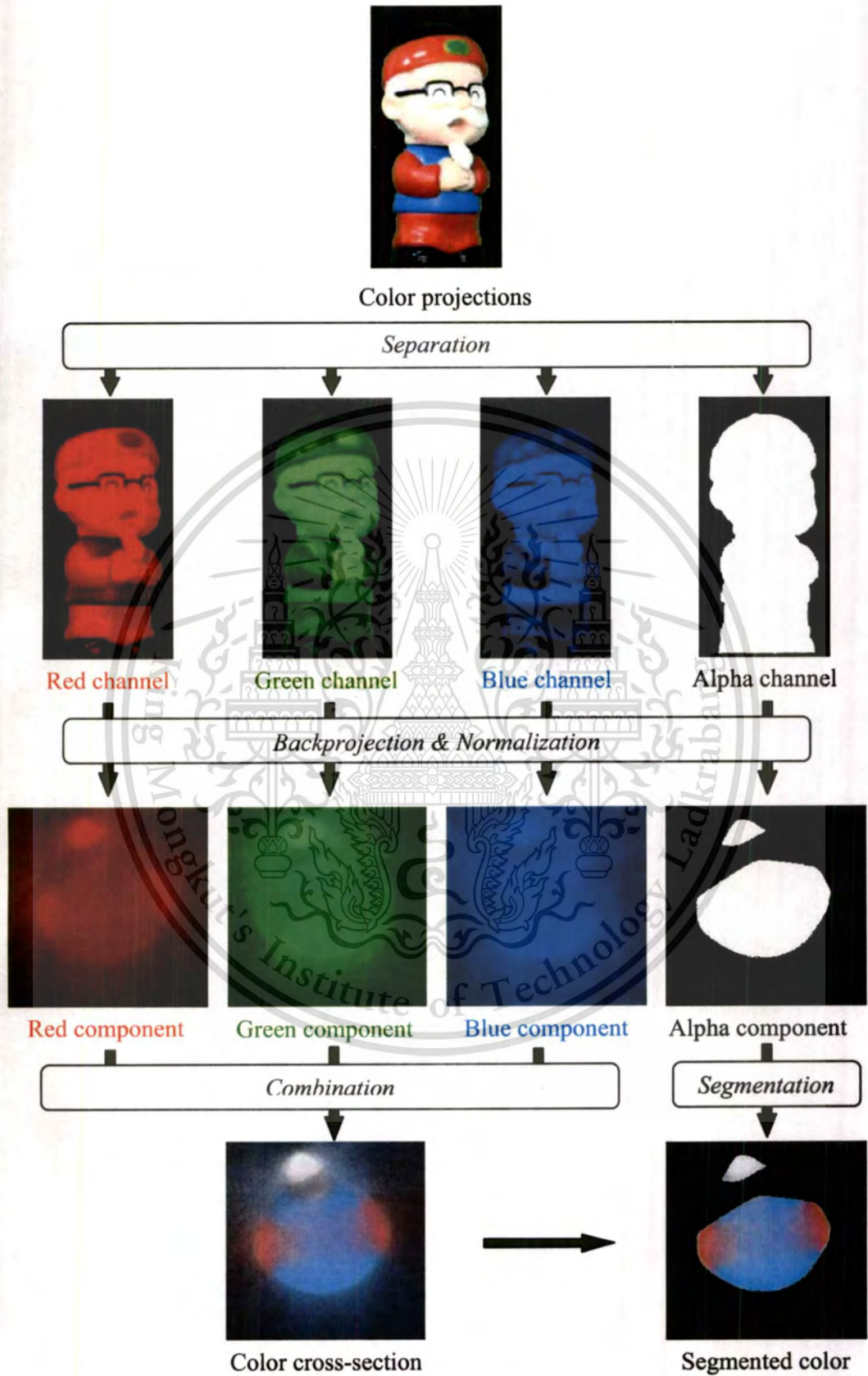


Fig. A.1 Reconstruction of the color cross-section in an RGB mode

This material is reserved for educational use only, not allowed for commercial use.

Forbidden to modify the content, and cite the document when use.

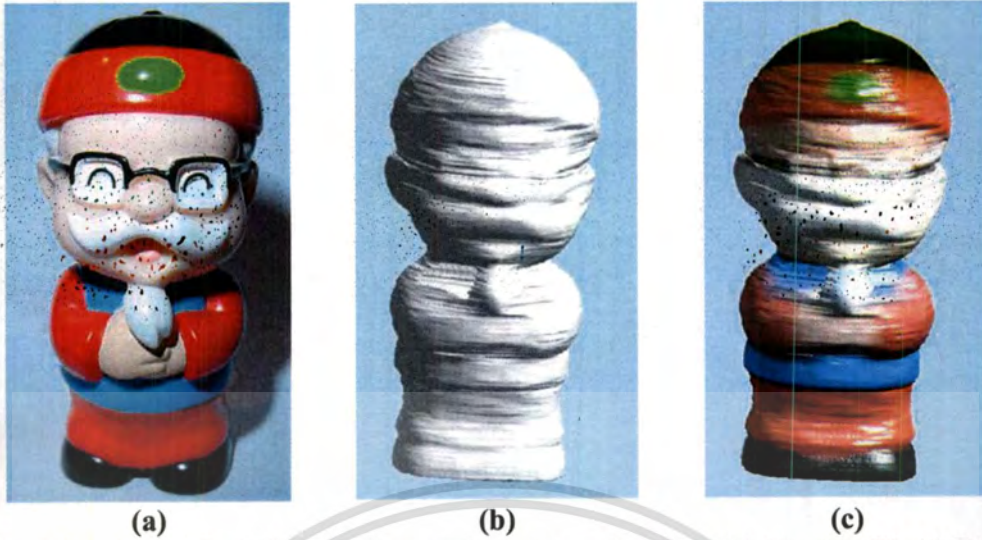


Fig. A.2 (a) original, (b) colorless, and (c) true-colored model (Az.170,El.-10,Tw.-5)

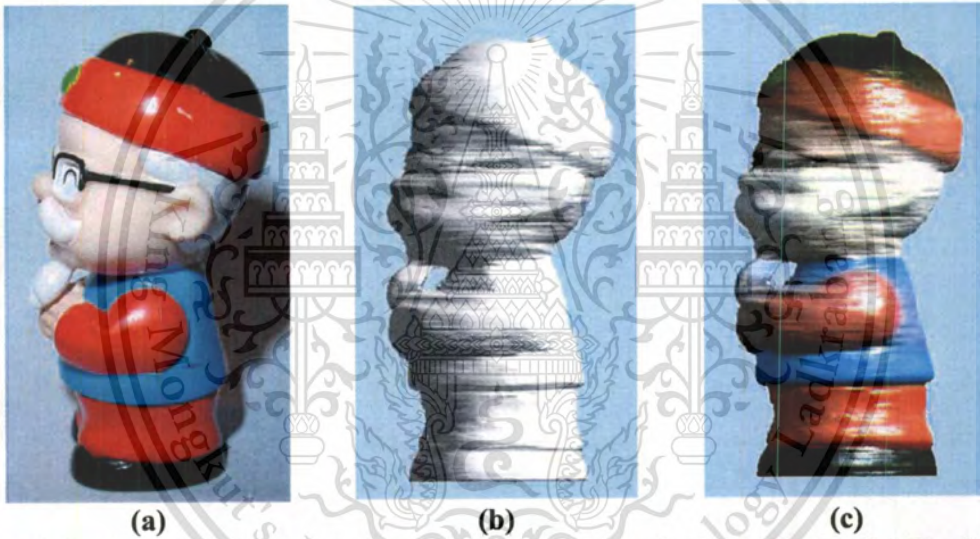


Fig. A.3 (a) original, (b) colorless, and (c) true-colored model (Az.95,El.0,Tw.0)

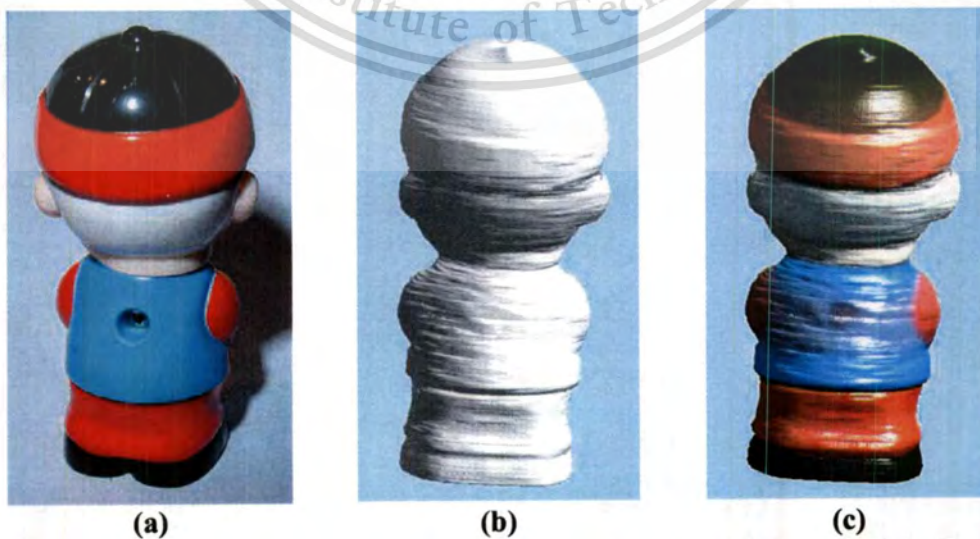


Fig. A.4 (a) original, (b) colorless, and (c) true-colored model (Az.-10,El.10,Tw.-5)

This material is reserved for educational use only, not allowed for commercial use.

Forbidden to modify the content, and cite the document when use.

Autobiography

Born in Bangkok on December 20, 1980, I received the second-class honor in bachelor's degree of engineering (Electronics) from King Mongkut's Institute of Technology, Ladkrabang in 2000. Afterwards, I enrolled in the master course of engineering at the same place with the major in electronics in the field of biomedical image processing. In addition, I worked as an assistant researcher for the project of *Image Reconstruction from Ultrasonic Wave*, and an instructor for the undergraduates in the electronic laboratory.

The publications I have submitted during the master course are as follows:

- [i] C. Pintavirooj, W. Withayachumnankul, S. Tungjitkusolmun, and K. Chitsakul, "3D Shape Recovery Based Radon Transform," *Proc. International Symposium on Communications and Information Technology*, Chiang Mai, Thailand, November 2001. pp. 377-380.
- [ii] W. Withayachumnankul, C. Pintavirooj, M. Sangworasil, and K. Hamamoto, "3D Shape Recovery Based on Tomography," *Proc. International Conference on Signal Processing*, Beijing, China, October 2002, pp. 784-787.
- [iii] W. Withayachumnankul, K. Hamamoto, C. Pintavirooj, and P. Suwanna, "A Computational Analysis of Ultrasonic Reflection Mode Tomography Using Frequency-Shift Method," *Proc. International Symposium on Communications and Information Technology*, Phattaya, Thailand, October 2002, pp. 174-177.
- [iv] C. Pintavirooj, T. Rattana, W. Withayachumnankul, and M. Sangworasil, "3D Modeling Using Cone-Beam Tomography," *Proc. International Symposium on Communications and Information Technology*, Phattaya, Thailand, October 2002, pp. 178-181.
- [v] W. Withayachumnankul, A. Romputtal, C. Pintavirooj, and S. Taertulakarn, "An Investigation on Ultrasonic Attenuation Tomography Using the Integrated Power Spectrum Ratio Method," *Proc. International Congress on Biological and Medical Engineering*, Singapore, December 2002.

Any comment or query should be sent directly to withawatw@yahoo.com